

HOWARD SETYAMUKTI

800223

MODERN METHODS IN LIGHT
MICROSCOPY



Report

Mathematisch-Naturwissenschaftliche Fakultät

Institut für Biochemie und Biologie

CONTENTS

| | | |
|----|---|----|
| 1 | LIGHT SHEET MICROSCOPY | 1 |
| 2 | MICROPHOTOGRAPHY | 4 |
| 3 | LASER SCANNING MICROSCOPY | 10 |
| 4 | TOTAL INTERNAL REFLECTION FLUORESCENCE MICROSCOPY | 20 |
| 5 | EXPANSION MICROSCOPY | 22 |
| 6 | AIRYSCAN | 24 |
| 7 | DECONVOLUTION | 27 |
| 8 | CA-IMAGING | 33 |
| 9 | FLUORESCENCE CORRELATION SPECTROSCOPY | 36 |
| 10 | FLUORESCENCE RECOVERY AFTER PHOTOBLEACHING | 46 |
| | References | 50 |

1

LIGHT SHEET MICROSCOPY

1.1 INTRODUCTION

AIM To study the features of Light Sheet Microscopy method in image acquisition.

Light sheet microscopy is a technique to achieve high resolution optical sectioning and named so to reflect the mode of illumination in which a sheet of light illuminates plane(s) in the sample. This mode of illumination coming from the side of detection ensures signal arises only from in-focus regions and reduces exposure of other areas [1]. The comparison of this mode of plane illumination to the point illumination in confocal laser scanning microscopy (LSM) is shown in Fig. 1.

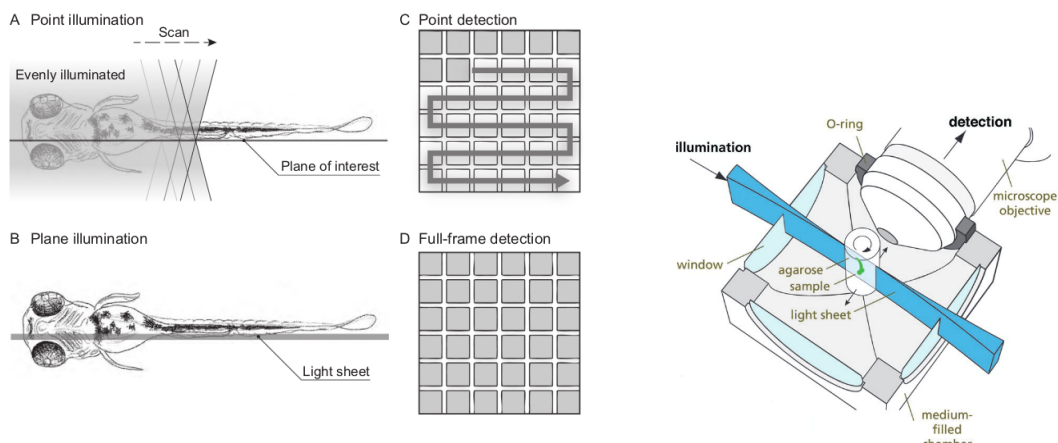


Figure 1: Comparison of point illumination in conventional confocal technique and plane illumination in light sheet microscopy (from Weber et al [2]).

Figure 2: Schematic of light sheet microscopy (adapted from Huisken et al [3]).

The advantage of plane illumination is immediate, namely only a specific plane being illuminated, in contrast to LSM where a significant part of the specimen being illuminated, even when imaging only a single plane (Fig. 1 A&B). Furthermore, the detection mode in LSM where the laser is scanned across the plane for image acquisition is disadvantageous in respect to acquisition time in comparison to light sheet that allows the whole frame to be acquired at once (Fig. 1 C&D).

1.2 METHODS

The device used for this experiment is a horizontal microscope Zeiss Lightsheet.Z1 with temperature regulated sample chamber and filled with medium (water). The detection is orthogonal against the illumination plane (Fig. 2.)

The specimen is put into a capillary filled with low melting agarose and then placed in the chamber. The sample is then positioned to face the imaging lens at an

angle (to minimize light path through agarose). Fluorescence excitation is by blue laser (488 nm), and images are recorded at 16 bits.

The samples in this experiment are the autofluorescent *Eleocharis acicularis* and *Egeria densa* (*Elodea*).

1.3 RESULTS AND DISCUSSION

The obtained maximum intensity projection of both samples are presented in Fig. 3. Due to the advantage of Light Sheet Microscopy, imaging was done relatively quick as a full frame of a z-stack could be obtained almost instantly as compared to other high resolution methods, chiefly LSM.

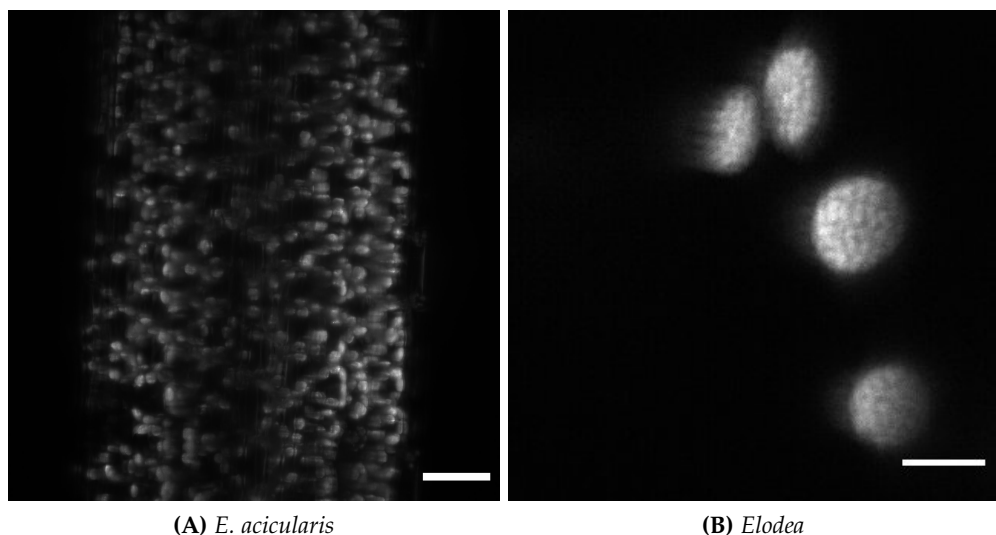


Figure 3: Maximum intensity projections of *E. acicularis* and *Elodea* specimen. Objective lens: Plan Apochromat 20×/1.0 UV Vis for both images. Scalebar is 30 µm on A and 5 µm on B.

The fact that illumination comes in a certain direction (either left or right) means that some structure could stand as a hindrance that casts a “shadow” that would obscure another structure behind it from being properly illuminated. For this, the device allows the option to “pivot” the sample called the *Pivot Scan* that moves the sample slightly (in a rotating motion) to minimize this shadowing effect. This can be seen by comparing the images presented in Fig. 4A & Fig. 4B where structures can be obscured by shadows and pivoting the sample slightly could minimize the effect and allows a back-positioned structures to be illuminated and observed as well.

In this image (Fig. 4) some stripping artifacts could be also observed. These artifacts is the result of features that scatter or absorb the light resulting in weaker illumination, visible as stripes. A solution for this is by obtaining several z-stacks at different angles. Then a composite of these z-stacks can be created using algorithms. However this would increase acquisition time dramatically and exposes the sample to a higher amount of illumination [4].

The two illumination sources (from the left and right side of the sample) aim to ensure that both sides of the sample can be evenly exposed to illumination, to deal with the fact that if the illumination comes only from one side, e.g. left, the far side of the sample (right) would be exposed to less amount of illumination in comparison

to the near side. The use of dual illumination should in theory reduce the stripping artifacts, however not significantly enough in this case.

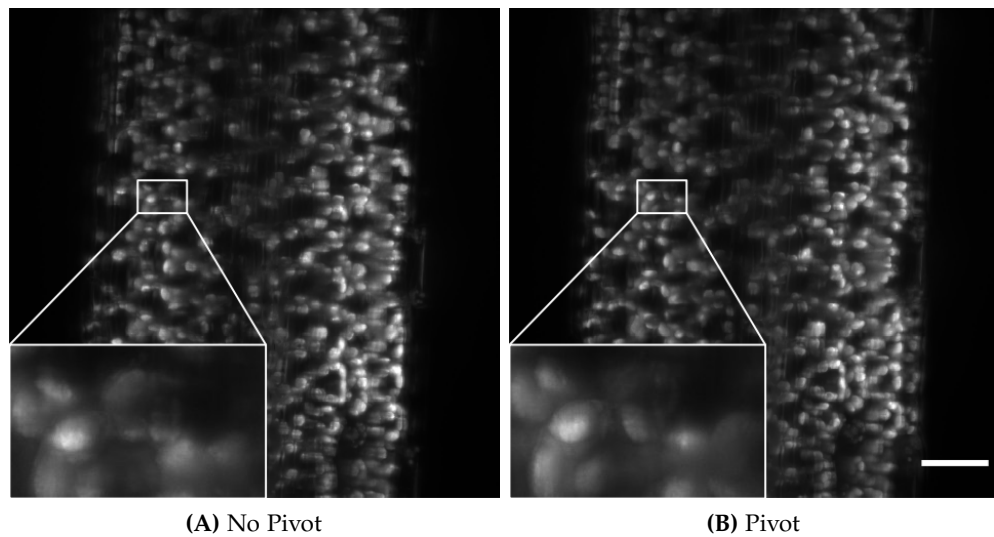


Figure 4: Pivot scan comparison of *E. acicularis*. Inset shows an example of where the illumination of a structure is hindered by another structure in front of it and pivoting the sample minimize this effect. Objective lens: Plan Apochromat 20 \times /1.0 UV Vis. Scalebar is 30 μ m.

Light sheet microscopy also minimizes photodamage due to the reduction of exposure in other areas and hence suitable to image live cells, along with the fact that the device is equipped with other support systems (e.g. temperature regulation). A time series image was recorded in which the chloroplast of *Elodea* could be observed moving around in Fig. 5.

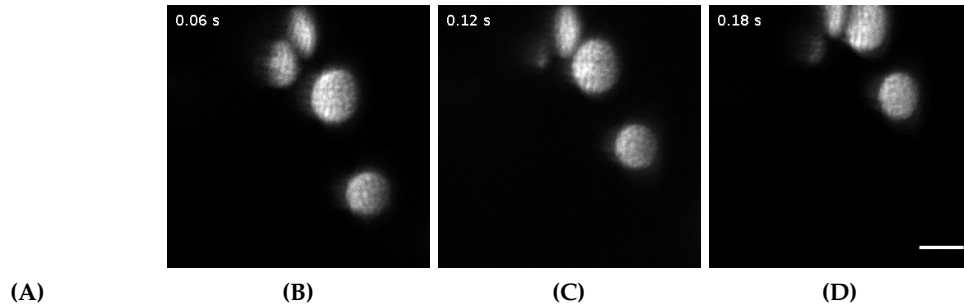


Figure 5: Movement of chloroplast in *Elodea* captured in 10 frames (t: 0.00-0.18 s). **A** is animated (Best viewed on Adobe Acrobat Reader, for other pdf-reader, please follow this [link to an external webpage](#) or alternatively, open the accompanying animated file.), **B-D** show some selected frames. Scalebar is 5 μ m.

2

MICROPHOTOGRAPHY

2.1 INTRODUCTION

AIM To identify the characteristics, advantages, and disadvantages of various wide-field microscopy methods.

2.2 METHODS

Several different microscopes were utilized during this experiment corresponding to the type of technique that was used for imaging.

Generally, sensitivity during imaging was adjusted to 400. However this changes from time to time according to the brightness of the images obtained. For example, sensitivity was increased to around 1600 for dark specimens (e.g. in fluorescence imaging). Illumination for all microscopy methods were generally set at around +2. For darkfield observations, the condenser was changed because the Numerical Aperture (NA) of the objective must be smaller than the NA of the condenser. Three lenses were utilized, namely: Plan neofluar $40\times/0.75$ Ph2 for most imaging experiments, Achromplan $40\times/0.6$ Korr for darkfield microscopy, and Plan Apochromat $63\times/1.4$ Oil DIC for imaging using oil immersion.

2.3 RESULTS AND DISCUSSION

Images presented in this report are processed accordingly. Most images are greyscale and contrast enhanced for visualization purposes. Contrast enhancement for the most part of this experiment is achieved by normalization (contrast stretching/histogram stretching) process with 0% saturation to make sure that the data are kept with minimal change. The same visualization result could be achieved by manually adjusting the minimum and maximum displayed pixel values (brightness/-contrast), this is shown in Fig. 2.3.1. However, this normalization procedure allows a more straightforward workflow with a stricter procedure and maintain easier reproducibility.

Two findings of using this procedure: One, this procedure does not significantly improve the quality of some images, e.g. darkfield images, which has already good contrast. Nevertheless this method was done to such images anyway due to the workflow and the results are not at all detrimental for visualization and assessment. In other words, no significant differences could be observed between the normalized ones and the ones adjusted manually (compare Fig. 2.3.1B and Fig. 2.3.1C).

Two, this procedure were successful in enhancing the contrast for almost all other images except for some. Closer investigation of the histogram and pixel values of these images in detail (e.g. blowfly fluorescence) found that there are some outliers at high pixel values. This is demonstrated by saturating (during normalization) at

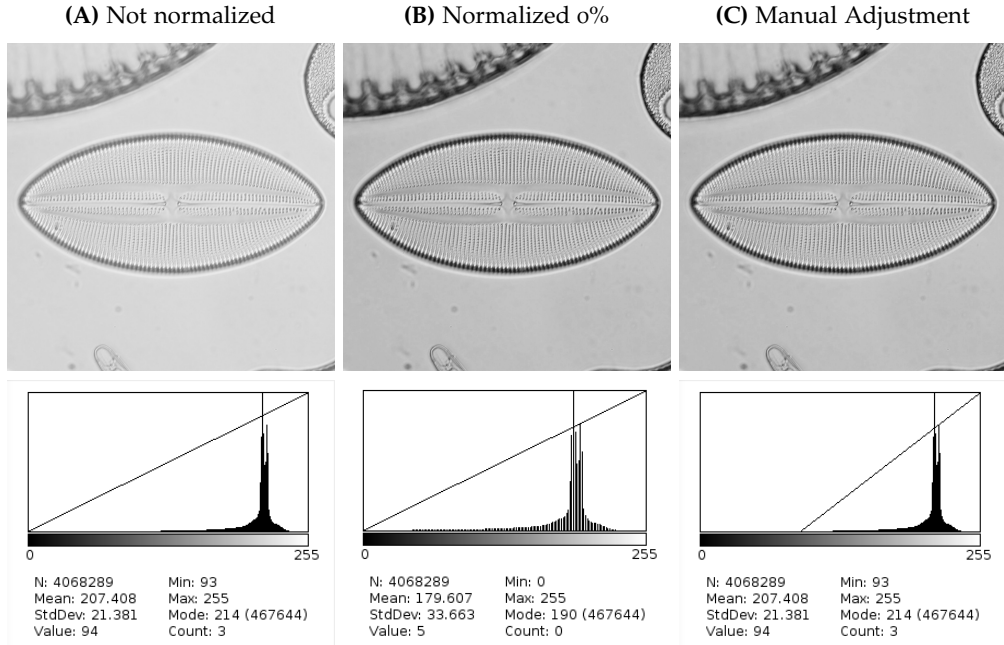


Figure 2.3.1: Example of contrast enhancement by normalization. Diagonals in the histograms are added manually, no scale bar presented, images are for illustrative purposes only.

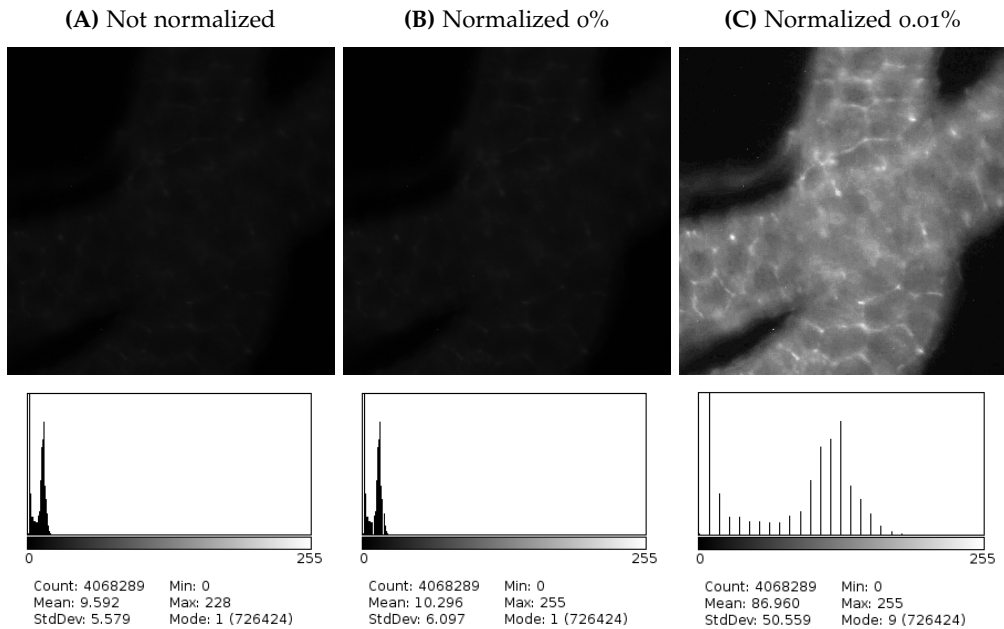


Figure 2.3.2: Example of removing outlier values by normalization. No scale bar presented, images are for illustrative purposes only.

really low percentage (0.01%) removes the outliers and enhanced the contrast significantly. As can be seen in Fig. 2.3.2. The grey-scaled but unnormalized image (Fig. 2.3.2A) of blowfly fluorescence is very dark and contrast enhancement is necessary. Applying the procedure without saturation (Fig. 2.3.2B) does not improve the contrast at all. Just by adjusting the saturation to 0.01% (Fig. 2.3.2C) the contrast is improved dramatically. For consistency reasons, all images acquired from the same technique are treated the same, although this may not be strictly necessary. How-

ever since the saturation amount is practically negligible, this should not hinder the purpose of visualization of the images in this report.

2.3.1 Diatoms

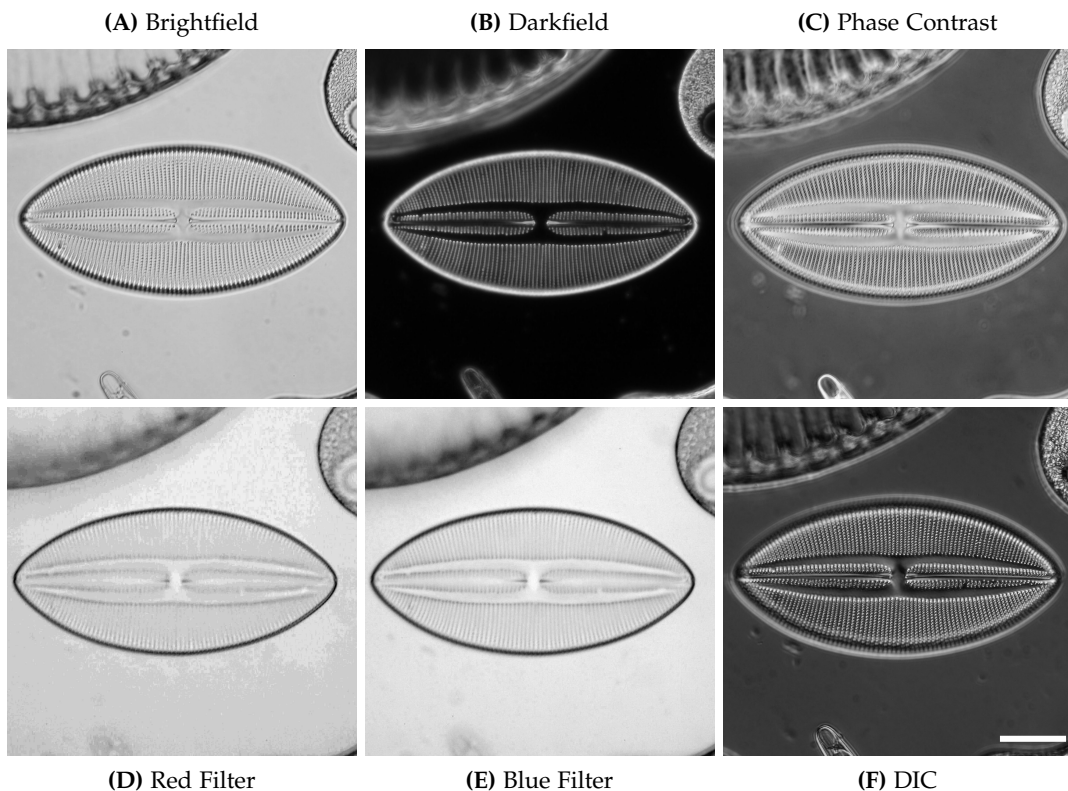


Figure 2.3.3: Comparison of diatom (*N. lyra*) images using brightfield, darkfield, phase contrast, and DIC microscopy. Additionally, brightfield microscopy was also conducted using blue and red filters. A, C, D, E, and F used Plan Neofluar $40\times/0.75$ Ph2 lens, B used Achromplan $40\times/0.6$ Korr lens. Scalebar is 25 μm .

Fig. 2.3.3 shows images of a diatom (*Navicula lyra*) taken with different techniques. As can be seen in the Fig. 2.3.3D & 2.3.3E, the resulting images look comparatively grainy. Normalization without saturation of the grey-scaled images performed poorly due to outliers for both these images. Therefore, saturation was set to 0.01% to improve the contrast, though graininess was then introduced to the image. However, also apparent in these images, that light with longer wavelength (e.g. red light, Fig. 2.3.3D) does not show minute structures of the diatom well, in comparison to blue light (Fig. 2.3.3E) which has shorter wavelength. The shorter wavelength of blue light are scattered more strongly by smaller structures (or particles) than the longer wavelength red light, hence the less obvious structures of the diatom when viewed with red light/filter. Both of these lights compose the light for brightfield microscopy (Fig. 2.3.3A), which gives just as detailed an image as its is for darkfield microscopy (Fig. 2.3.3B), just inversely illuminated. However, the darkfield images are arguably advantageous in this case due to the fact that since the specimen is unstained, more contrast can be obtained this way in comparison to brightfield microscopy. Other methods to obtain even more contrast were also performed, namely; phase contrast microscopy, whose image in Fig. 2.3.3C shows a glowing halo around the specimen,

and DIC - Differential Interference Contrast (Fig. 2.3.3F) which displays the characteristic pseudo-3D effect.

It can also be illustrated by this specimen the effect of NA on resolution. Fig. 2.3.4 shows how the minute structures are more easily resolved by higher NA lenses. Although the techniques used are different, but the effect can still be clearly observed [5].

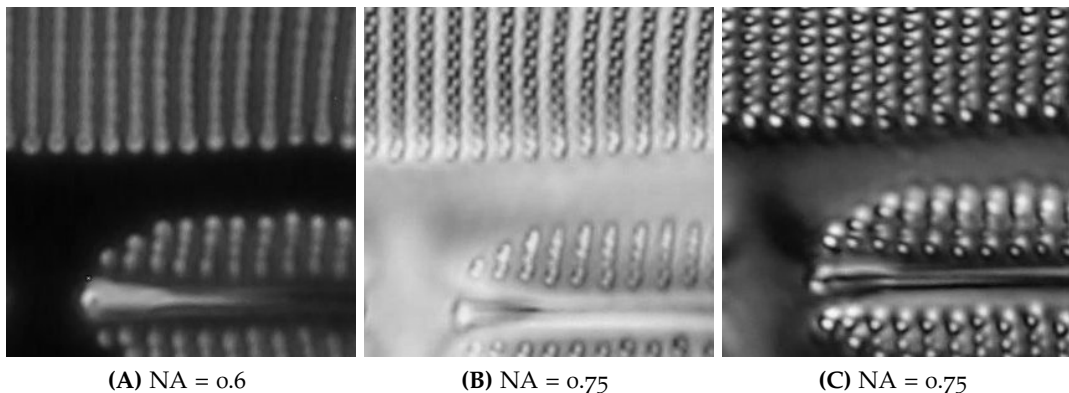


Figure 2.3.4: Comparison of the effect of different NA on resolution. Zoomed in images of the same diatom specimen. A used Achroplan $40\times/0.6$ Korr lens, B and C used Plan Neofluar $40\times/0.75$ Ph2 lens. No scale bar presented, images are for illustrative purposes only.

2.3.2 Bloodsmear

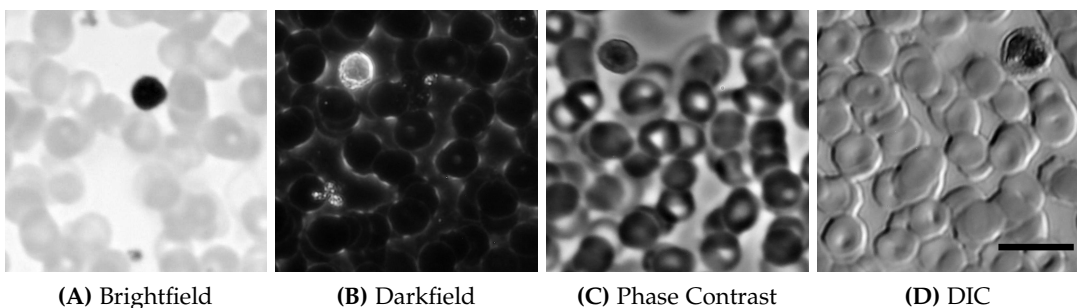


Figure 2.3.5: Bloodsmear specimen under brightfield, darkfield, phase contrast, and DIC microscopy. A, C, and D used Plan Neofluar $40\times/0.75$ Ph2 lens, B used Achroplan $40\times/0.6$ Korr lens. Scalebar is $15\ \mu\text{m}$.

In the bloodsmear specimen, all imaging methods (Fig. 2.3.5) could help distinguish red blood cells among white blood cells. The darkfield image (Fig. 2.3.5B) seems to display this most prominently, other than the fact that the contrast between the background and other cells looks very poor.

The phase contrast and DIC (Fig. 2.3.5C & 2.3.5D) method allow a better resolution of the cells between each other and also against the background in comparison to the brightfield (Fig. 2.3.5A) and darkfield microscopy.

2.3.3 Blowfly salivary gland

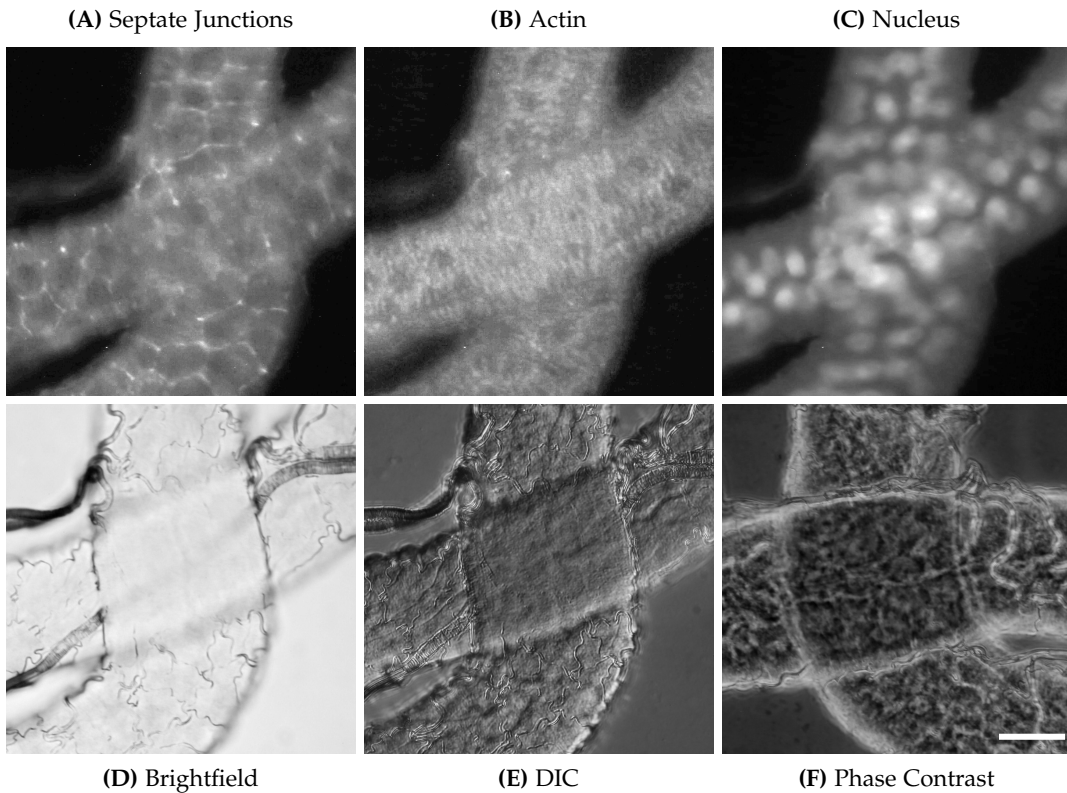


Figure 2.3.6: Blowfly under fluorescence, brightfield, DIC, and phase contrast microscopy. Septate junctions labelled by immunofluorescence (AlexaFluor568), actin by AlexaFluor488-Phalloidin, and the nucleus by DAPI. Objective lens: Plan Neofluar $40\times/0.75$ Ph2. Scalebar is $25\text{ }\mu\text{m}$.

The blowfly salivary gland specimen was labelled using three different fluorescent markers, namely; DAPI, AlexaFluor488-Phalloidin, and immunofluorescence against FasIII. Each of the label binds to certain part of the salivary gland. These fluorescent labels can be excited by light with the corresponding excitation wavelength. Immunofluorescence of Fasciclin III on the septate junctions of the cell utilizes green excitation and produces red emission (Fig. 2.3.6A). The green emission of AlexaFluor488-Phalloidin (Fig. 2.3.6B) is excited by blue excitation light, and shows the actin filaments of the cell. The round structures in Fig. 2.3.6C shows the nucleus of the cell, in which DAPI binds to DNA and emits blue emission. All these organelles would otherwise be hardly visible in the brightfield microscopy (Fig. 2.3.6D). DIC and phase contrast microscopy (Fig. 2.3.6E & 2.3.6F respectively) provide a more detailed look into the specimen and reveal structures which in brightfield microscopy can only be hazily visible.

2.3.4 Pinewood and Starch

In Fig. 2.3.7A, the brightfield microscopy of pinewood, one can vaguely observe the pits of pinewood that connects one cell's walls to the other. Other than generating more contrast, DIC and polarization microscopy allow more fine structures to be observed. The birefringent pits (pairs) can be identified more clearly by using

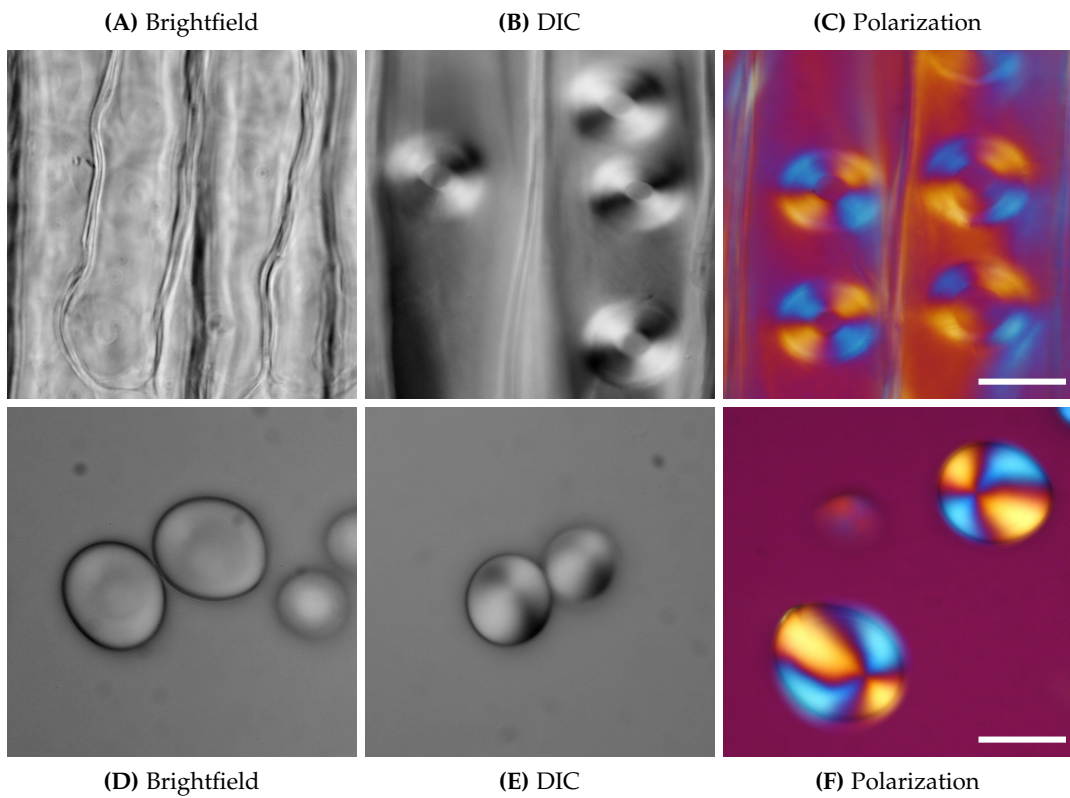


Figure 2.3.7: Pinewood (top row) and starch (bottom row) specimen under brightfield, DIC, and polarization microscopy. Objective lens: Plan Apochromat 63 \times /1.4 Oil DIC. Scalebars are 20 μm for both specimens.

either DIC or polarization microscopy (Fig. 2.3.7B & 2.3.7C). Furthermore, polarization microscopy by using a gypsum platelet red 1st order (λ plate) in a crossed position (Fig. 2.3.7F) allows even more information to be obtained regarding the negative birefringency of pinewood or conversely, positive birefringency for the rod mixed body of starch granules [6]. This can be identified by the orientation of the yellowish-orange and blue color.

3

LASER SCANNING MICROSCOPY

3.1 INTRODUCTION

AIM (BASIC) To get to know basic Laser Scanning Microscopy (LSM) functions.

AIM (MULTIFLUORESCENCE) To investigate multifluorescent specimens, spectral analysis, and 3-D imaging.

Confocal Laser Scanning Microscopy (Confocal LSM/CLSM/Confocal/LSM) is a high-resolution optical imaging technique. This technique utilizes a pinhole at the focal point to remove fluorescence emissions originating from planes other than the one in focus, although regions that do not directly contribute to the useful signal are still exposed to excitation light, which may lead to photodamage.

It works by acquiring fluorescence signal in a scanning manner, i.e. point-by-point in a line, and line-by-line in a plane to produce a high resolution 2D image. Since this imaging technique results in a very thin slice of image (axially), imaging different planes and combining them can produce a 3D image of a specimen.

3.2 METHODS

3.2.1 Basic LSM

To familiarize basic LSM functions, several images of the rhizome of lily of the valley specimen were taken. Most images were taken using the objective lens EC Epiplan Neofluar $20\times/0.5$ DIC M27, unless otherwise stated. Obtained images were then coded in 16 bits and then compared to observe the effect of different pinhole sizes, scanning speeds, laser intensities, NA, and digital resolutions.

3.2.2 Multifluorescence, Spectral Analysis, and 3-D Imaging

Several different specimens are investigated in this section, namely: bovine endothelial cells, cross section of the rhizome of Lily of the valley, algae and diatoms, cells from a blowfly's abdomen, blowfly salivary gland, and a gold covered coverslip. The particular techniques are discussed in the following section in more detail. The objective lenses used are: Plan-APOCHROMAT $63\times/1.4$ Oil, Plan-Neofluar $20\times/0.5$, and C-APOCHROMAT $\times/1.2$ 1mm. Full-Width at Half-Maximum (FWHM) calculations are done in Python (script available publicly on GitHub, or by request).

3.3 RESULTS AND DISCUSSION

3.3.1 Basic LSM

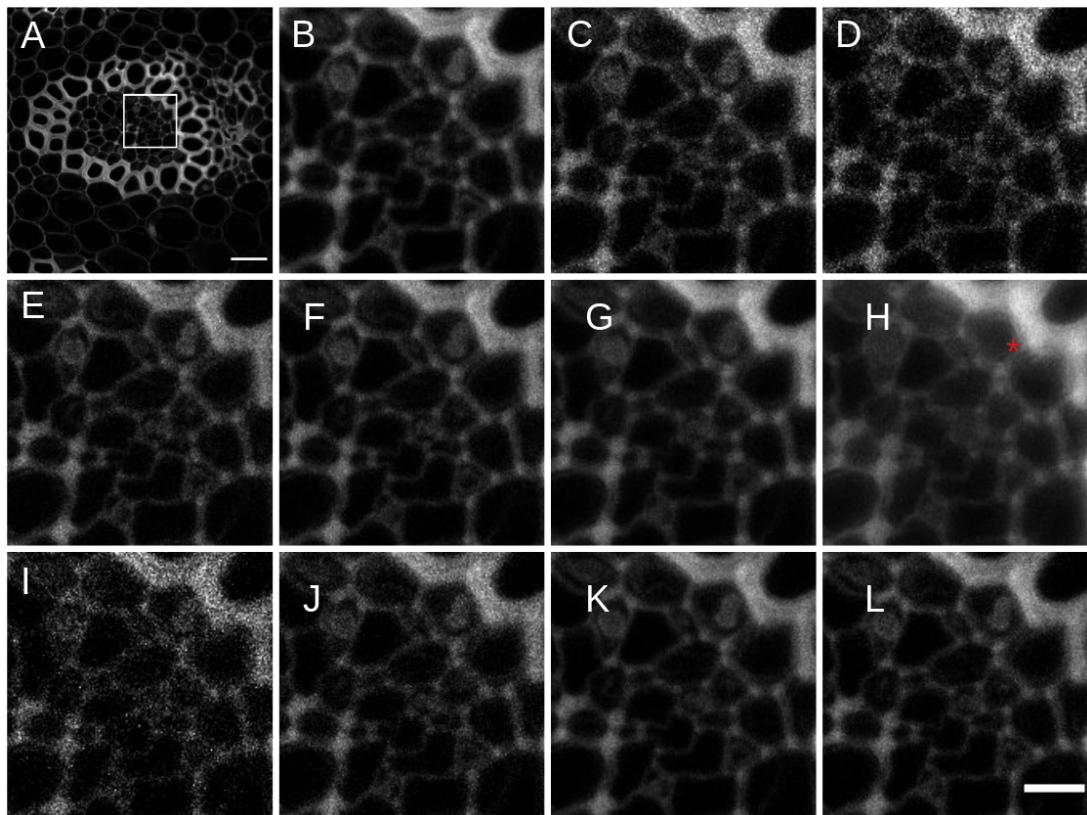


Figure 3.3.1: Lily of the valley specimen. A: original image with white square marking the magnified area. B-D are the sample imaged with varying scanning speed, E-H with varying pinhole sizes, I-L with varying laser intensity. B: Minimum scanspeed, C: Medium scanspeed, D: Maximum scanspeed. E: Pinhole 0.5 AU, F: Pinhole 1 AU, G: Pinhole 2 AU, H: Pinhole maximum. I: Laser 0.5, J: Laser 2, K: Laser 2 (with averaging 4), L: Laser 5. Objective lens: EC Epiplan Neofluar 20 \times /0.5 DIC M27. Scalebar on original image is 30 μ m, on the zoomed in image is 10 μ m. Red asterisk shows the disappearance of the small structure.

To compare how different scanning speed may have influence on imaging, acquisition was done using different scanning speeds. Fig. 3.3.1B-D shows the effect of scanning speed of Lily of the valley specimen (Fig. 3.3.1A). As can be seen, slower scanning speed allows for a higher resolution image and increasing the scanning speed reduces the resolution of an image and makes the zoomed-in image heavily pixelated, however this also makes the imaging process faster. A slower scanning speed could be advantageous in yielding a higher resolution image, however this increases the time required to conduct the imaging and also the risk of photobleaching the specimen.

The pinhole is a hallmark of a confocal microscopy system, it allows for the removal of emissions that do not come from the focal plane. The size of the pinhole generally should be exactly the size of the Airy disc [7], given in Airy Units (AU). Enlarging the pinhole allows for more extrafocal contribution to reach the detector, increasing the blurriness by signals from other planes. Decreasing the size would in theory allow the minimal extrafocal signal, and hence the thinnest focal plane. But

closing the pinhole would defeat the purpose of imaging afterall. The effect of different pinhole sizes can be seen in Fig. 3.3.1E-H. Larger pinhole makes image more blurry due to the reason mentioned before. The blurriness would hinder proper identification of structures as pointed by the red asterisk in Fig. 3.3.1H.

Shown in Fig. 3.3.1I-L are the images taken with different laser intensity (0.5, 2, 2 with averaging, and 5). The intensity of laser to use during imaging depends on the specimen being imaged and the setting of the imaging device. A sensitive specimen may not be able to be subjected to high intensity laser, which may destroy fluorescent species or the structure itself. A low intensity laser, on the other hand, may not produce enough energy to be detected by the light detector in the device. For this, the gain setting (amplification of input signal - increase the brightness of light features) and offset setting (zeroing the background level - set the darkest part to black) has to be set properly to compensate the weak signal to the surrounding noise (Signal to Noise ratio - SNR). Hence, for sensitive specimen, a low intensity laser that does not destroy the specimen would require a compensating gain and offset setting. The SNR in this case may not be the best.

Comparing the images taken using laser intensity 2 with and without averaging (Fig. 3.3.1J&K) shows the effect of it. The particular function takes the average of a longer sampling time when imaging. A longer sampling time (more signal acquisition), or higher averaging level would lead to better SNR because more frames are gathered and averaged. This is evident from (Fig. 3.3.1K&L) where averaging gives a clearer image with a lot less noise than without. Since the Lily of the valley specimen used in this experiment autofluoresce and almost impossible to bleach, a higher averaging level would be preferable to obtain a smoother image. But otherwise, for more sensitive specimen, a longer sampling time may be disadvantageous.

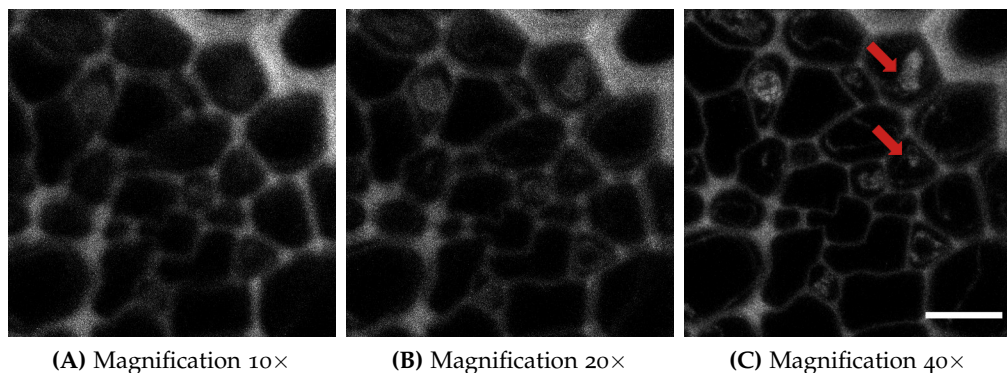


Figure 3.3.2: Lily of the valley specimen imaged using different magnification on the same image plane. Digital resolution of original images are 1024×1024 . Shown here are insets corresponding to the image in Fig. 3.3.1A. Objective lens: A: EC Plan neofluar $10\times/0.3$ M27, B: EC Epiplan Neofluar $20\times/0.5$ DIC M27, C: EC Plan neofluar $40\times/1.3$ Oil DIC. Scalebar is $10\text{ }\mu\text{m}$. Red arrows show smaller structures that are visualized more clearly.

Fig. 3.3.2 shows the effect of different magnifications on a sample. It can be observed that higher magnification yields better imaging result for smaller structures, demonstrated visually in Fig. 3.3.2C with the smaller structures shown more clearly pointed by the red arrows. The magnification is a property of the utilized objective lens and is strongly related to the NA. The higher the NA of a lens, the clearer an image is. The NA is, however, determined by the refractions index and angle of the cone of light. To increase the NA, and hence the optical resolution, a higher

refractions index is desireable. This can be achieved by using a different medium ($NA_{air} \approx 1$, $NA_{water} \approx 1.3$, $NA_{oil} \approx 1.5$; depending on λ). Of course, the objective must be suitable for the preferred medium.

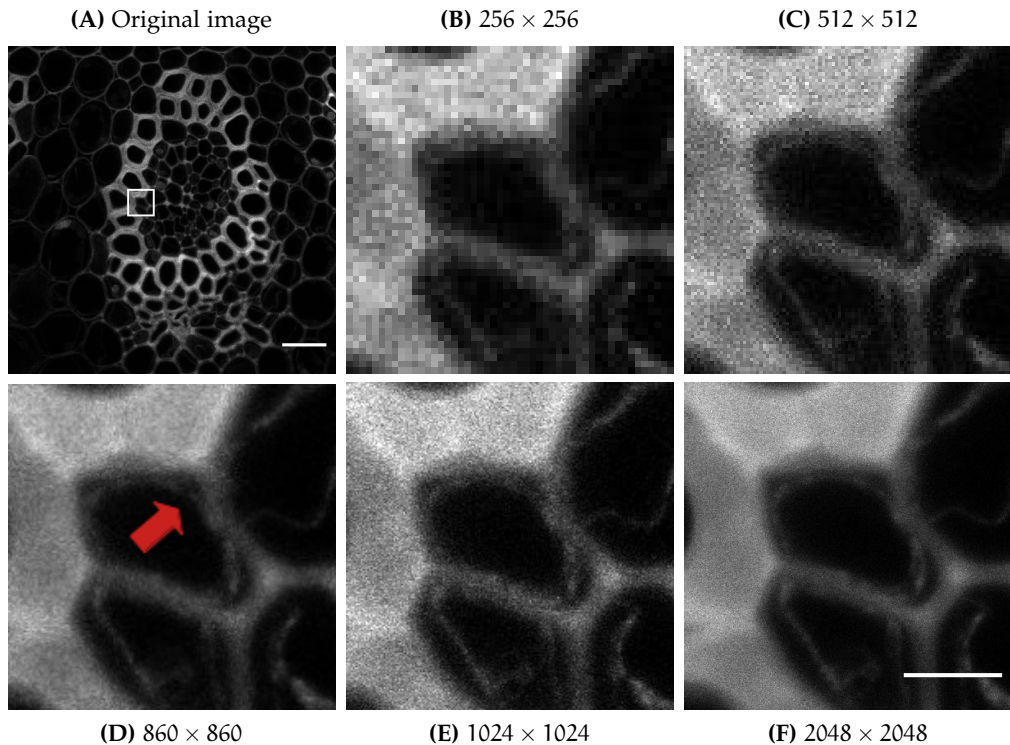


Figure 3.3.3: Lily of the valley specimen pictured with different digital resolutions. White square on the original image marks the magnified area. Objective lens: EC Plan neofluar $40\times/1.3$ Oil DIC. Scalebar on original image is $30\text{ }\mu\text{m}$, on the zoomed in image is $5\text{ }\mu\text{m}$. Thick red arrow shows smaller structures that can be distinguished more clearly.

The effect of different image (digital) resolution can be seen in Fig. 3.3.3. The optical resolution of a digital image depends on the sampling interval to make an accurate representation of the real features of a specimen. To maintain the spatial resolution of an image, according to Nyquist criterion, the sampling interval has to be equal to twice the highest spatial frequency of the specimen [8]. Any lower than this, then features with higher spatial frequency will not be readily resolvable, as shown by the red arrow in Fig. 3.3.3D, which shows a smaller structure that can start to be resolved on a digital resolution at least 512×512 (more clearly seen on 860×860), which would otherwise be unresolved (indistinguishable with neighbouring structures) on resolutions lower than that. For live cell imaging sessions however, the Nyquist criterion may have to be violated in order to maintain the well being of the specimen.

Fig. 3.3.4A shows the Maximum Intensity Projection (MIP) of the sample. The maximum intensity projection results in a brighter and clearer image of every structure because it adds the intensity of every layer of the stacked images. As mentioned before, the confocal technique allows for optical sectioning, in which a specimen can be imaged layer-by-layer along the axial- or z-axis. The combined result of this layer-by-layer imaging produces a 3D image of the specimen. Fig. 3.3.4B shows one perspective of the acquired image. This image is obtained by making a so-called z-stack acquisition of the specimen.

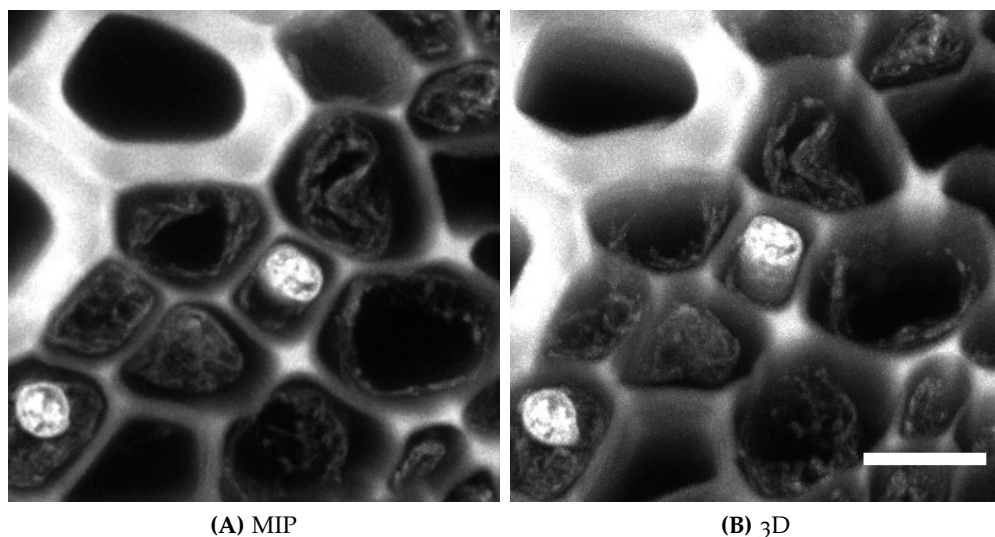


Figure 3.3.4: Lily of the valley specimen, Maximum intensity projection and 3D picture (one perspective). Objective lens: EC Plan-Neofluar $40\times/1.3$ Oil DIC. Scalebar is $10\ \mu\text{m}$.

3.3.2 Multifluorescence, Spectral Analysis, and 3-D Imaging

Some investigations may require multiple labelling of a specimen to observe different parts of the cell and it is advantageous to simultaneously image this multiply labelled specimen in contrast to doing it sequentially. However, problems may arise due to signal interference (also called crossover, bleed-through, or crosstalk) when the fluorescence signal is close to each other. This phenomenon is demonstrated in Fig. 3.3.5 that shows multiply labelled bovine endothelial cells. The top row shows imaging in single track mode, where DAPI signal bleeds through to AlexaFluor488-Phalloidin channel (Fig. 3.3.5A-C) but not to the Mitotracker channel. This is confirmed by removing the excitation on 405 nm (Fig. 3.3.5D) where the bleed-through is removed. Some strategies can be employed in approaching such a problem, namely by means of mathematical approach that involves applying algorithms termed *channel unmixing* [9][10]. This method does not really work because the algorithm functions on where the intensity is the highest, and in this case, it is on where the nucleus is, therefore it is necessary to decrease DAPI excitation. The result can be seen in Fig. 3.3.5E where the bleed-through is significantly reduced although some traces can still be recognized along with some dark spots that seems to trace the mitotracker signal. Another approach is by using multitracking option to enable fast switching between laser lines using an Acousto-Optic Tunable Filter (AOTF) to separate excitation (and the subsequent gathering of fluorescence emission) of each fluorophore [11]. The result in Fig. 3.3.5F shows no bleed-through that can be observed.

A linear unmixing method that can be employed to separate fluorescence signals that are close to one another is the Automatic Component Extraction (ACE) in which a Lambda stack is acquired. The Lambda stack is a collection of whole images taken with incrementing wavelength ($\pm 10\text{ nm}$ apart.). Usually, spectral information are directly searched from the Lambda stack by inspecting all channels for regions within where no signal is detected in the other channels. That region is then assigned as pure fluorophore/regarded as reference and can be used for the unmixing operation. If such region is not found, then the area with the lowest signal intensity in the other channels is assigned to be a reference. This is how ACE works and is mathemati-

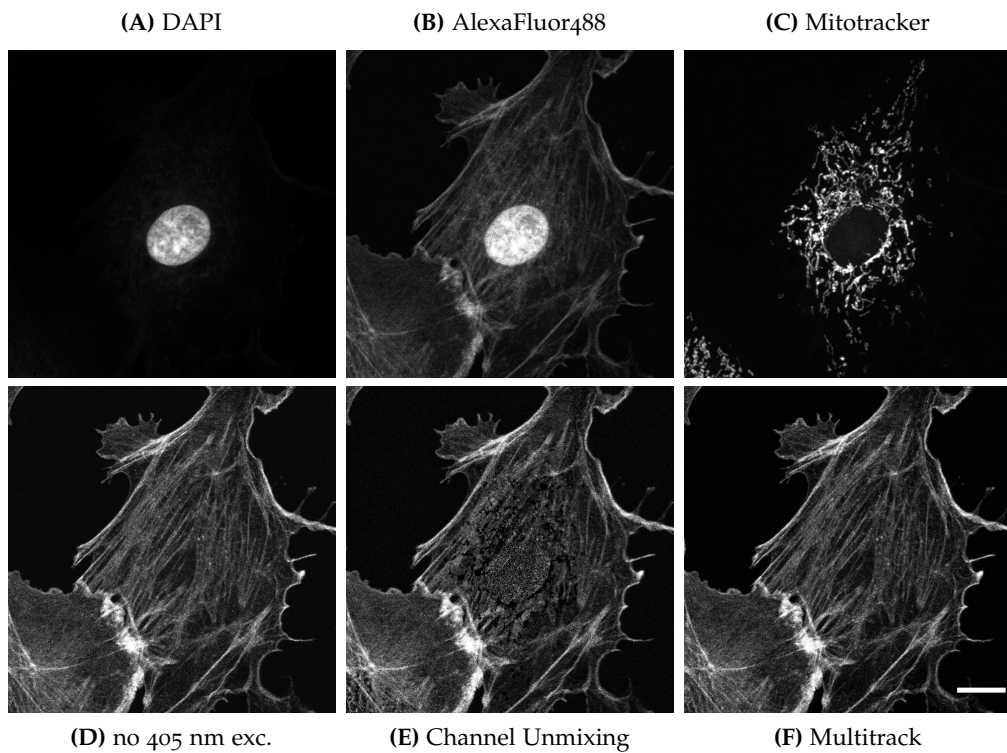


Figure 3.3.5: Top row: 3 channels of bovine endothelial cells image acquisition labelled by: DAPI that binds to the nucleus, AlexaFluor 488-Phalloidin that binds to the actin filaments, and Mitotracker RedCMXRos that binds to mitochondria using single track acquisition. Bottom row: Images of the channel AlexaFluor488: without 405 nm excitation, using channel unmixing, and multi-tracking. Objective lens: Plan Apochromat $63\times/1.4$ Oil. Scalebar is $10\text{ }\mu\text{m}$.

ally based on Principal Component Analysis (PCA) [12]. In Fig. 3.3.6-Top is shown the resulting ACE of a lily of the valley specimen. Simply inspecting the composite image, it can be seen that the image is dominated by channel 3 and 1. Comparing channel 2 and 3 suggests that channel 2 is similar to channel 3 but less complete and most likely does not carry significant information not contained in channel 3. This can indeed be seen by inspecting the fluorescence spectra where the spectra of channel 2 and 3 lie close together.

Another channel produced by this function is the residual channel (channel 4) which consist of spectral signals that do not match those in the reference library and hence not assigned. This could be signals that arise from saturated pixels or from high background levels [12]. Ideally, no signal should be exhibited in this channel. Signals shown in this channel indicates the quality of the ACE process is not optimal.

Instead of producing the reference spectra automatically, manually selecting regions in a sample to be designated as a reference is also possible to do. This of course depends a lot on the sample itself, whether it contains regions that exhibit pure fluorescence or not and also the individual eye of the operator. In Fig. 3.3.6-Bottom is shown the result of the online fingerprinting function that captures the image by using the reference spectra that are manually selected. This function does not require the recording of a lambda stack to be performed prior to acquisition, but necessitates reference spectra that can either be manually selected or recorded separately. It can be seen here that channel 1 of the manual selection managed to isolate

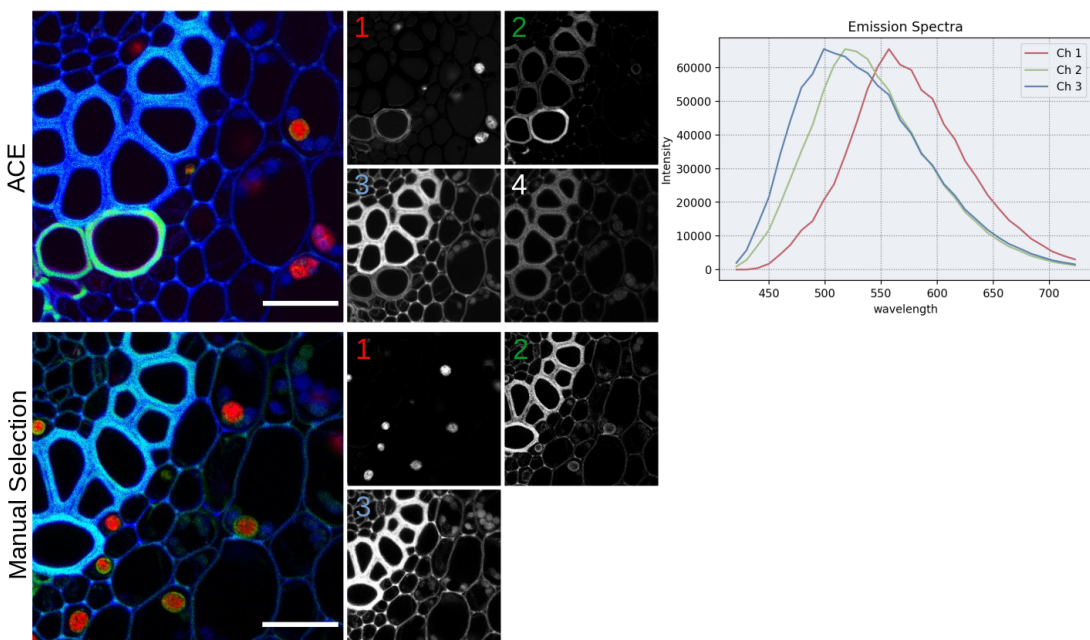


Figure 3.3.6: **Top:** Composite result of ACE with the channel breakdown on the right of it (excluding channel 4, which is the residual channel). The fluorescence spectra of channel 1-3 is shown on the far right. **Bottom:** Composite result of online fingerprinting function by manual selection of reference spectra on sample. On the right of it are images of the channel breakdown. Objective lens: Plan Neofluar 20 \times /0.5. Scalebars are 30 μ m.

the information of the bead-like structures in comparison to the channel 1 of ACE that includes information regarding the cell walls as well. This bead-like structures could be nutrients/glucose stored as starch in the form of intracellular granules. The comparison of channel 2 and 3 of manual selection seem to show that they carry similar information of the cell walls, but differs rather prominently in regards of the granules. This can probably be explained by the fact that autofluorescent samples do not exhibit a well defined fluorescent signal/peaks which poses a difficulty in selecting a region of pure fluorescence and hence suboptimal result.

In principal, a sample that contains regions with well defined fluorescent signal can be easily worked with either manually or automatically, with the advantage that automatic procedures saves time and effort. But whenever this is not possible, or the resulting component extraction does not seem to be optimal, a manual selection may be warranted, although not without its own pitfalls.

Another option would be to obtain reference from another sample that contains a well defined signal and save the spectra as a standard reference. In this case, care must be taken that measurement conditions of the reference sample is identical to the measurement conditions of the investigated sample.

The phenomenon of autofluorescence can be exhibited by a variety of organisms. Shown in Fig. 3.3.7 is the autofluorescence of a live sample of algae and diatoms taken from the pond. It can be seen here that there are algae that have similar fluorescence spectrum with diatoms and other algae that do not.

As mentioned previously, confocal technique/LSM also allows for imaging a specimen in 3-D. Fig. 3.3.8 shows a comparison of four representation options of a 3-D image acquisition (z-stack) of the rhizome of a lily of the valley specimen. Maximum intensity projection (Fig. 3.3.8A) is very simple, depth is intuitively recognizable, and still maintains the sense of 3-D of the structures despite the simplicity. It is the

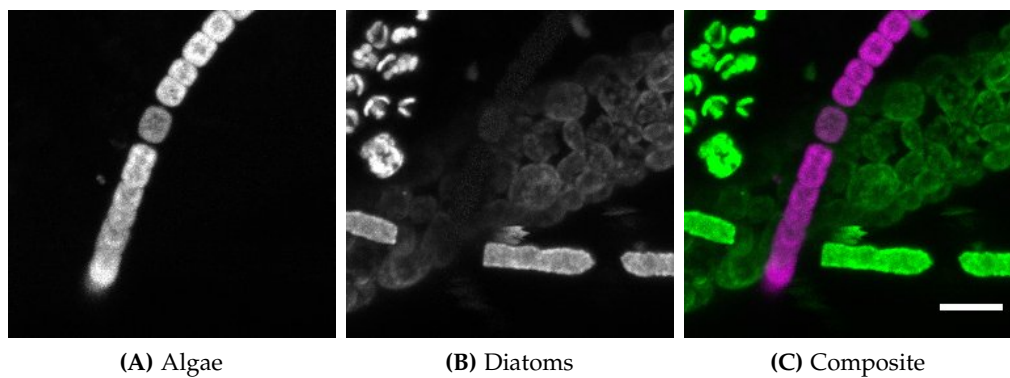


Figure 3.3.7: Algae and diatoms autofluorescence. Objective lens: C Apochromat 40 \times /1.2 Imm water immersion. Scalebar is 10 μm .

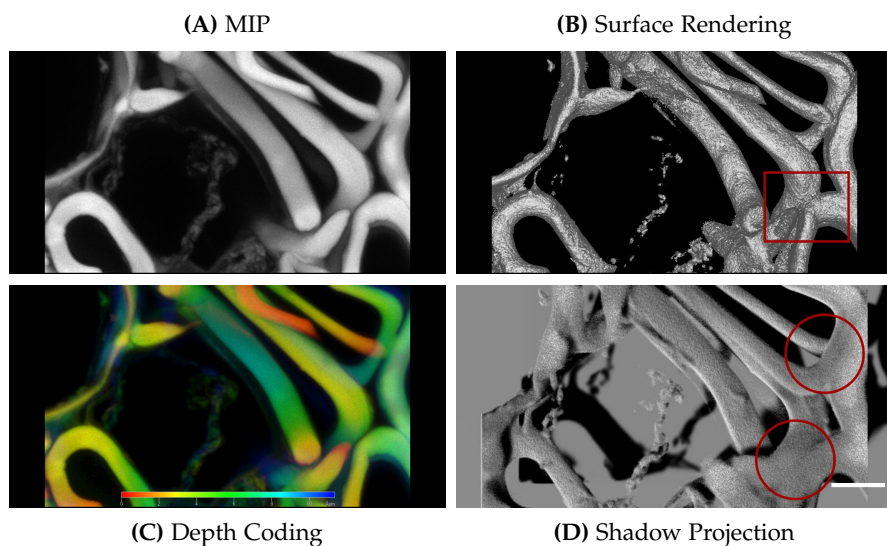


Figure 3.3.8: 3D representation of a cross section of the rhizome of a lily of the valley specimen. Objective lens: Plan Apochromat 63 \times / 1.4 Oil. Scalebar is 5 μm . Areas enclosed by red square/circle represent area(s) that are challenging to interpret.

most commonly used representation. Surface rendering approaches may introduce some texture on the surface of structures which could make recognition difficult as indicated by the red rectangle in Fig. 3.3.8B. Depth coding (Fig. 3.3.8C) emphasizes in providing depth information, however it is not as simple as maximum intensity projection due to the fact that most of the information is carried by colors (which necessitates the use of one). Depending on the case, some purpose may require the use of this method. Shadow projection offers a strong sense of three-dimentionality, however some parts can be easily obscured as demonstrated by the red circles in Fig. 3.3.8D.

A z-section made by the previous image acquisition is shown in Fig. 3.3.9A. This presentation shows a rather compressed z-section. Applying corrections by adapting the z-step length to the pixel size in x-y, Fig. 3.3.9B is obtained which shows a more appropriate dimension, although it is apparent that the top part of the specimen receives more excitation and exhibits a stronger fluorescence response. Adjusting auto z-brightness correction (Fig. 3.3.9C) allows for a more evenly distributed signal to deal with the fact that fluorescence response gets weaker the deeper a layer is located.

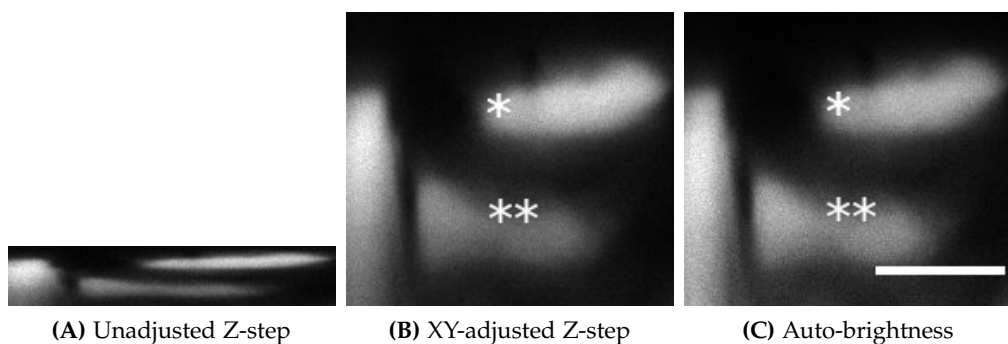


Figure 3.3.9: Z-section of the rhizome of a lily of the valley specimen. White star symbols aids the comparison of fluorescence signal strength. Objective lens: Plan Apochromat 63 \times /1.4 Oil. Scalebar is 5 μ m.

ated. This can be seen clearly by inspecting Fig. 3.3.9B and 3.3.9C together with the white star symbols as a comparison. It can be seen that without the auto-brightness adjustment, the top part of the image exhibit more fluorescence signal than the part below it. With the auto-brightness adjustment, the bottom part of the image shows a relatively more balanced signal.

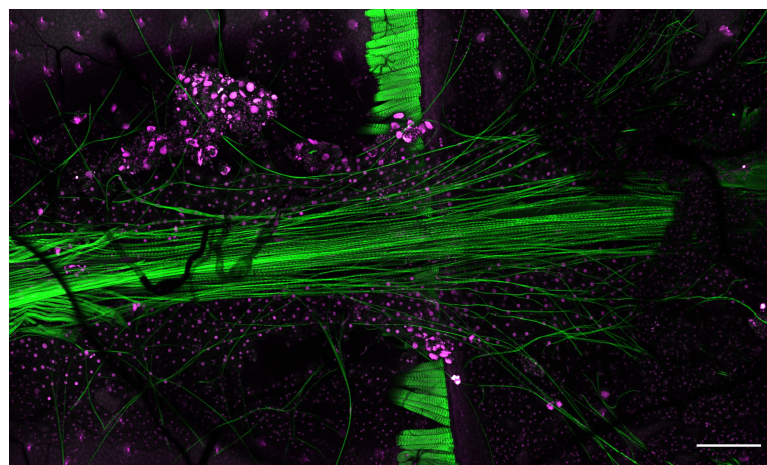


Figure 3.3.10: A large area of a blowfly abdomen (heart) specimen. Green is actin labelled by AlexaFluor 488-Phalloidin, and blue is nucleus labelled by DAPI. Objective lens: Plan Neofluar 20 \times /0.5. Scalebar is 150 μ m.

Sometimes, the area one would like to capture is larger than the scan area offered by the device. The option *Tile Scan* allows for imaging a large area of a specimen by moving the scan area and stitch them together automatically. The acquired large-area image of a blowfly abdomen (heart) is shown in Fig. 3.3.10.

Fig. 3.3.11 shows a 3-D perspective of a z-stack image acquisition of a blowfly salivary gland where Fasciclin-III is labelled by anti-Fasciclin-III/AlexaFluor568-conjugated goat anti-mouse-IgG, actin is labelled by AlexaFluor488, and nucleus is labelled by DAPI, which is not visible perhaps due to the possibility that the nucleus has diffused out of the sample because the sample is old.

The pinhole size of a confocal microscopy affects not only in the xy-dimension, but also the resolution in the z-dimension, as can be seen in Fig. 3.3.12 that shows xz-section of a gold-covered coverslip, where the smaller pinhole size gives a better resolved image. This is confirmed as well by the calculation of the FWHM of the

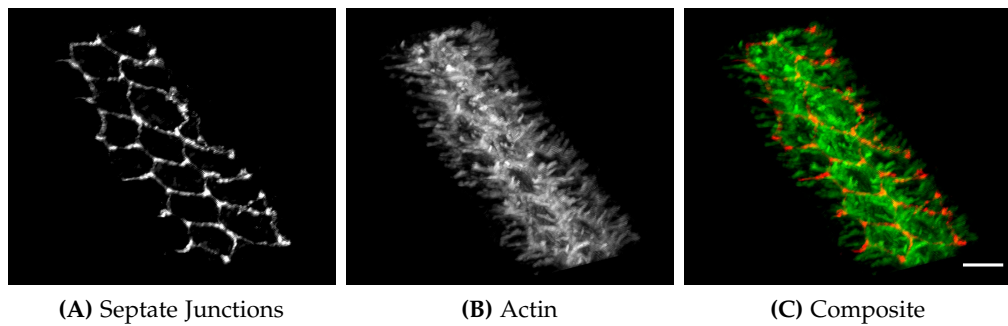


Figure 3.3.11: Blowfly salivary gland. Septate junctions labelled by AlexaFluor568, actin is labelled by AlexaFluor488. Objective lens: C Apochromat 40 \times /1.2 lmm water immersion. Scalebar is 5 μm .

acquisitions where the FWHM increases along with the increasing pinhole opening size. The FWHM calculation was done by a gaussian fit to the intensity-distance data of the acquisitions of each pinhole size with neither intensity normalization nor baseline correction. To note, the data for pinhole opening of 3 AU seems to be jeopardized, and hence excluded from calculation.

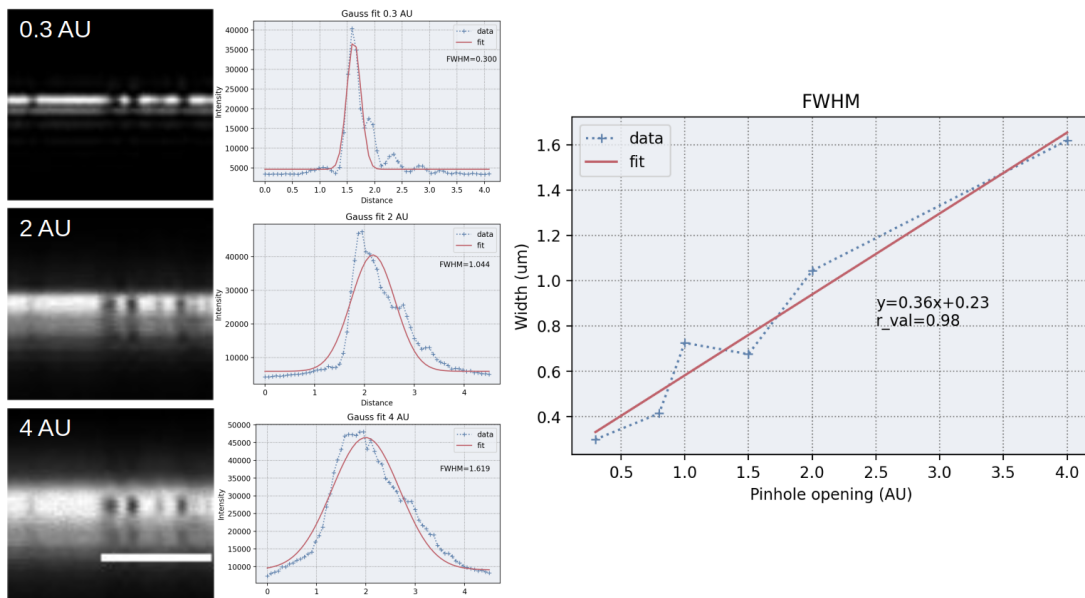


Figure 3.3.12: xz-section of a gold-covered coverslip with different pinhole sizes along with the gaussian fit to obtain the FWHM, and the relationship between it and pinhole sizes. Images were acquired with pinhole size 0.3, 0.8, 1, 1.5, 2, and 4 AU (here shown only a selection of those). Objective lens: Plan Apochromat 63 \times /1.4 Oil. Scalebar is 3 μm .

4

TOTAL INTERNAL REFLECTION FLUORESCENCE MICROSCOPY

4.1 INTRODUCTION

AIM To observe adhesion between cells and the contact between cell-surface.

Total Internal Reflection Fluorescence Microscopy (TIRF) allows imaging of fluorescent molecules located close to the glass/water (or glass/specimen) interface. Depending on the excitation wavelength and objective NA, the thickness of the excitation depth, which is called the evanescent field, can be less than 100 nm from the solid surface. In comparison, the thickness of a confocal image section is approximately 500 nm [13]. However the disadvantage is that the section is confined to a single-plane immediately adjacent to the glass [14].

In TIRF, excitation light is beamed through a glass substrate in direction of an aqueous specimen at a certain angle called the critical angle, at which total internal reflection occurs. This is due to the difference of refractive index between glass and water. This produces an evanescent wave (an electromagnetic field) in the aqueous phase. The evanescent field penetration depends on light wavelength, difference of refractive index, and the angle of incidence. Since the penetration of the evanescent field rapidly decays, only the fluorophores near the glass-liquid interface are excited, allowing a form of optical sectioning.

To reach an angle of incidence that is greater than the critical angle, TIRF microscopy requires a high NA (> 1.45). This can be achieved by using immersion oil.

4.2 METHODS

The specimen in this experiment is *Dictyostelium discoideum*, an amoeba, treated with the fluorescent marker Lim-GFP (Green Fluorescent Protein). This fluorescent marker is excited by blue laser (490 nm) and emits at 510 nm.

The measurement was conducted using the inverted microscope Olympus IX71. A semiconductor laser was used to excite the fluorescent marker during imaging.

4.3 RESULTS AND DISCUSSION

Lim-GFP is bound to the actin network of the cell due to the lim domain. Other parts of the cell can be marked using Lim-RFP. The size of this amoeba cell is normally 10-20 μm .

From a direct comparison between the images (Fig. 4.3.1) it can be seen that through normal mode, there are many that cells can be observed, however the TIRF mode only presents the cells, or a part (section) of the cells, that are *attached* to the slide, avoiding fluorescence excitation from other parts of the cell. Due to this, the images produced by this method have good signal-to-noise ratio with minimal fluor-

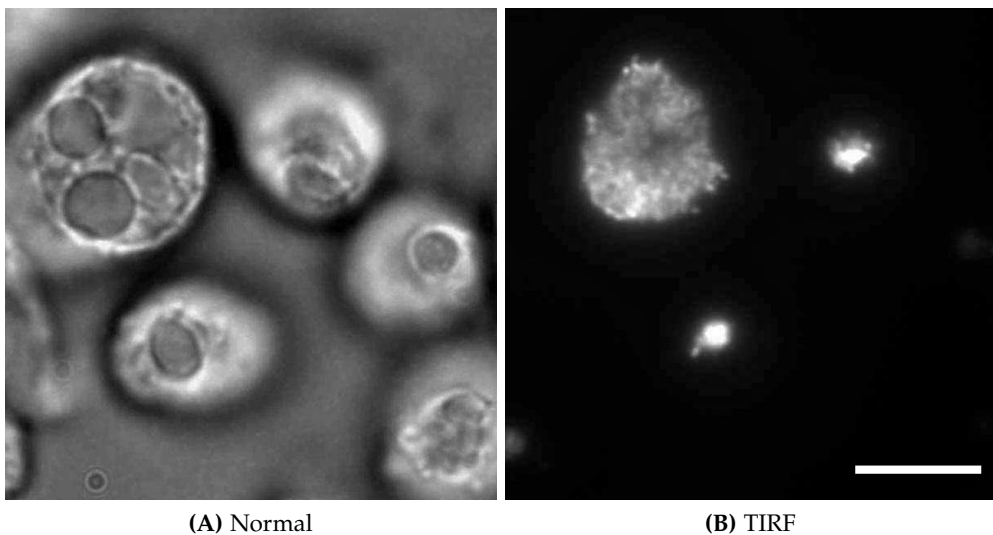


Figure 4.3.1: Side-by-side comparison of the same area of *Dictyostelium discoideum* imaged with normal and TIRF mode. Objective lens: UAPON 100 \times 1.49 oil immersion. Scalebar is 10 μm .

escence from out-of-focus planes. This is demonstrated by the vacuoles that can normally be seen in Fig. 4.3.1A. These vacuoles which are located usually around the center of cells are not observable anymore in TIRF mode (Fig. 4.3.1B).

The cells in the specimen were newly cultivated, which may account for the seemingly smaller size of the cells in the image. This may also play a part in the fact that the cells can move more freely and not very much attached to the slide. Since the cells were alive, the displacement of the cells can be observed during the imaging process when the experimenter changed the mode of imaging from normal to TIRF mode and adjusted the angle of reflection.

Comparing Fig. 4.3.1B and Fig. 4.3.2, the varying size of the cells are evident. On some of the cells, there are protruding parts that can be seen, these could be the pseudopods of the amoeba cells.

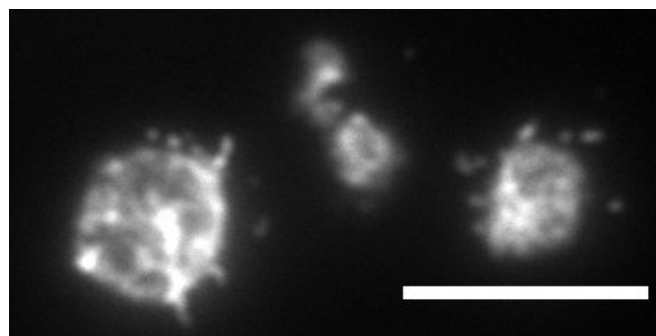


Figure 4.3.2: Another part of the same specimen. Objective lens: UAPON 100 \times 1.49 oil immersion. Scalebar is 10 μm .

5

EXPANSION MICROSCOPY

5.1 INTRODUCTION

AIM To enlarge a specimen by following an expansion microscopy protocol.

Expansion microscopy utilize a non-traditional approach to obtain a high resolution images. Instead of relying on state of the art devices to observe minute structures, this approach aims to magnify/expand the specimen itself and allows the observation to be conducted , in principle, using a conventional diffraction-limited microscopes. The use of a high resolution microscope would allow an even better observation. This expansion is achieved by means of linking a stained sample to a gel matrix that swells by absorbing water. The general scheme is shown in Fig. 5.1.1.

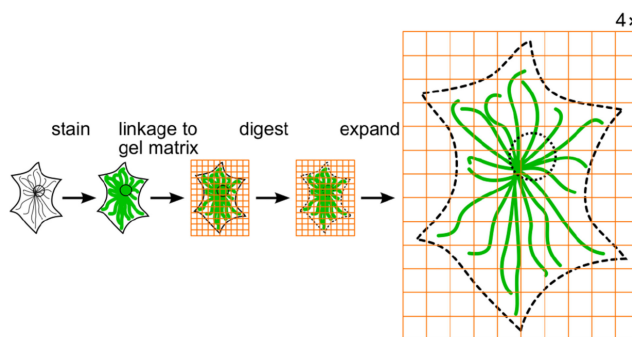


Figure 5.1.1: General scheme of expansion microscopy. Image adapted from Chen et al [15].

5.2 METHODS

Two samples of the AX2 line of *Dictyostelium discoideum* was stained, embedded to polymer matrix, digested, and expanded according to protocol (also made is a non-expanded control). The centrosome core (CP91) is labelled by AlexaFluor568 (red), the corona of the centrosome (CP224) by AlexaFluor488 (green), and nucleus by DAPI (blue).

5.3 RESULTS AND DISCUSSION

The calculation result of the expansion procedure of the gel matrix is shown in Fig. 5.3.1. As can be seen here, the expansion process succeeds in enlarging the gel matrix to more than 4 times the original size, and consequently, the cells embedded inside as well.

The resulting sample is then imaged by LSM, shown in Fig. 5.3.2. As can be inspected here, the resolution is increased dramatically. Comparison between Fig 5.3.2B

| | Pre-Expansion (cm) | Post-Expansion (cm) | Enlargement Factor |
|----------|-----------------------|------------------------|-----------------------|
| Sample 1 | a: 0.45 | A: 1.50 | $\sim 4.2 \times$ |
| | b: 0.60 | B: 2.70 | |
| | h: 0.75 | H: 3.30 | |
| | Area: 0.39 | Area: 6.93 | |
| Sample 2 | a: 0.65 | A: 2.50 | $\sim 4.3 \times$ |
| | b: 0.80 | B: 3.40 | |
| | h: 0.75 | H: 3.40 | |
| | Area: 0.54 | Area: 10.03 | |

Figure 5.3.1: **Left:** Schematic of the dimension of pre- and post-expansion gel matrix. **Right:** Table of measurement details (pre- and post-expansion) of both samples, including the area and enlargement factor.

to Fig 5.3.2F show that CP91 can be seen with a more prominent structure post-expansion. This is also the case in Fig 5.3.2G where it can be observed that CP224 can be captured showing more features instead of just a bright dot like in Fig 5.3.2C. It can also be seen a lot clearer here that the fluorescence label AlexaFluor488 sticking to the + ends of microtubules whereas in the control image these features are observable as a hazy cloud. The nucleus that is shown as being only a blurry cloud in Fig 5.3.2D can now be imaged with a much higher resolution as seen in Fig 5.3.2H.

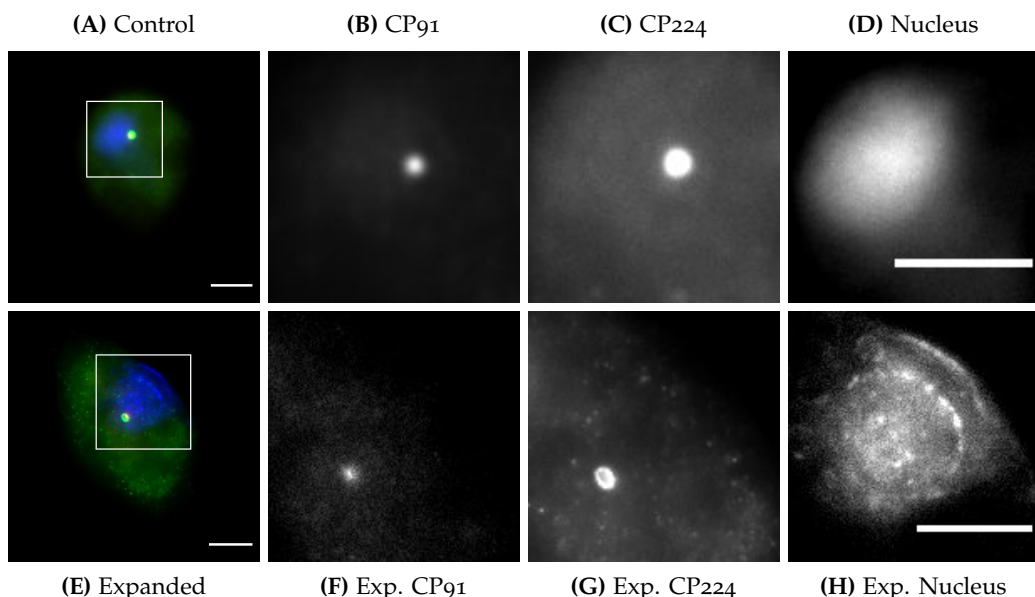


Figure 5.3.2: AX2 specimen composite and the magnified channel breakdown. White squares mark the magnified areas of images on the right of the composite. Control specimen at top row and expanded at bottom row. Shown here are single representative optical sections of a z-stack. Objective lens: Plan-Apochromat 100 \times /1.40 Ph3 oil immersion (control) and LCI Plan-Neofluar 63 \times /1.30 Imm Korr DIC water immersion (expanded). Scalebars are 3 μm for the control (both original and magnified images) and 10 μm for the expanded (both). Gamma correction of 1.50 was applied for all images.

6 AIRYSCAN

6.1 INTRODUCTION

AIM To study the features of Airyscan technology and compare with conventional confocal techniques.

The Airyscan method is similar to conventional confocal Laser Scanning Microscopy (LSM), however in this method, instead of using a physical pinhole, a special detector is utilized for the same purpose of confocal LSM. This Airyscan detector is a 32-channel gallium arsenide phosphide photomultiplier tube (GaAsP-PMT) area detector that collects a pinhole-plane image at every scan position [16].

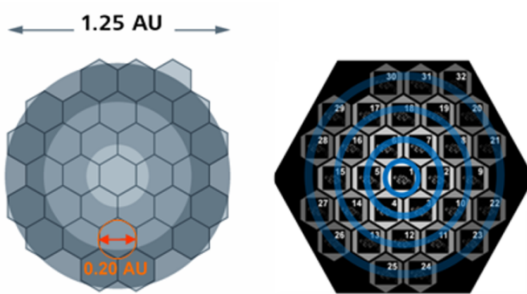


Figure 6.1.1: Airyscan detector. Image adapted from: <https://cif.unil.ch/the-airyscan-system-for-improved-confocal-resolution/>. Accessed: 02/01/2021.

This special detector (Fig. 6.1.1), which organized the area detector in a honeycomb-like structure (each detector acting as an individual pinhole with diameter 0.2 AU), and positioned in the conjugate focal plane (like the pinhole on conventional confocal microscopy) made it possible to collect more light (equivalent to a pinhole opened to 1.25 AU), and hence allows for an enhancement of resolution by the factor of 1.7 x and SNR by 4–8 times [17] in comparison to conventional confocal technique, where the downside to using a pinhole with a diameter less than 1 AU is the dramatic decrease in signal reaching the detector (95% loss at 0.2 AU) [16].

6.2 METHODS

The specimens used for this experiment are:

- Blowfly salivary gland. Actin labelled by AlexaFluor488-Phalloidin (green) and microtubules/septate junctions by anti-Na,K-ATPase ($\alpha 5$) / goat anti-mouse-IgG, AlexaFluor568-conjugated (magenta).
- AX2 line of *Dictyostelium discoideum* from expansion microscopy experiment. CP91 (centrosome core) labelled by AlexaFluor568 (magenta) and CP224 (centrosome corona) by AlexaFluor488 (green).

The device used in this experiment is Zeiss LSM-880 with an Airyscan detection unit, the objectives are $40\times/1.2$ lmm for the salivary gland and $63\times/1.3$ Oil immersion lens for the AX2 specimen.

The following was performed:

1. Airyscan acquisition
2. LSM acquisition with pinhole opening larger than 1 AU
3. LSM acquisition with twice the optimal number of pixels in the lateral dimension and half optimal distance in the axial dimension (then proceed with deconvolution)
4. Airyscan acquisition without module with pinhole size of 0.2 AU

The AX2 specimen was imaged only by Airyscan and LSM. The *Elodea* specimen listed for this experiment was dead and hence no data is available.

6.3 RESULTS AND DISCUSSION

Fig. 6.3.1 shows the resulting images of the salivary gland of a blowfly obtained using the previously mentioned methods. It can be seen here that the basolateral folds (apical membrane) can be seen better with the Airyscan than with LSM (Fig. 6.3.1 a₁&a₃). This is due to oversampling compared to the Nyquist criterion. This is also fairly observable by the blurriness of image Fig. 6.3.1 a₄ when it is quite clear in comparatively in image Fig. 6.3.1 a₂.

The constrained iterative deconvolution algorithm employed seem to improve the LSM imaging results (Fig. 6.3.1 a₅-a₇), but not quite to the degree of sharpness of Fig. 6.3.1 a₁. Another voluntary deconvolution method that was employed was inverse filter. This method does not perform as well as the previous method and seem to even introduce artifacts in the form of graininess, also evident in Fig. 6.3.1 a₈.

The removal of the Airyscan module (Fig. 6.3.1 a₉&a₁₀) warrants the compensation of reducing the pinhole size to 0.2 AU. This seem to result in an image that is in detail shows an increasing degree of blurriness/noise than the ones obtained with the module. This can be, for the most part, observed in the magenta (AlexaFluor568) channel. However the sharpness is still better than LSM with pinhole opening of 1 AU. This can also be seen in Fig. 6.3.1 a₁₀ in which the image still show a fairly sharp structures of the actins in comparison to Fig. 6.3.1 a₄, but not to the degree of Fig. 6.3.1 a₂.

The advantage of Airyscan compared to the more traditional LSM can be seen more clearly in the images of AX2 cells. Comparing both channels of CP91 and CP224 it is obvious that Airyscan (Fig. 6.3.2 b₁&b₂) gives a much higher resolution image with more readily observable structures and less murked by rough noise that is shown on LSM images. The sharpness of the centrosome corona (CP224) is also enhanced in Fig. 6.3.2 b₂ whereas it is very rough in Fig. 6.3.2 b₄.

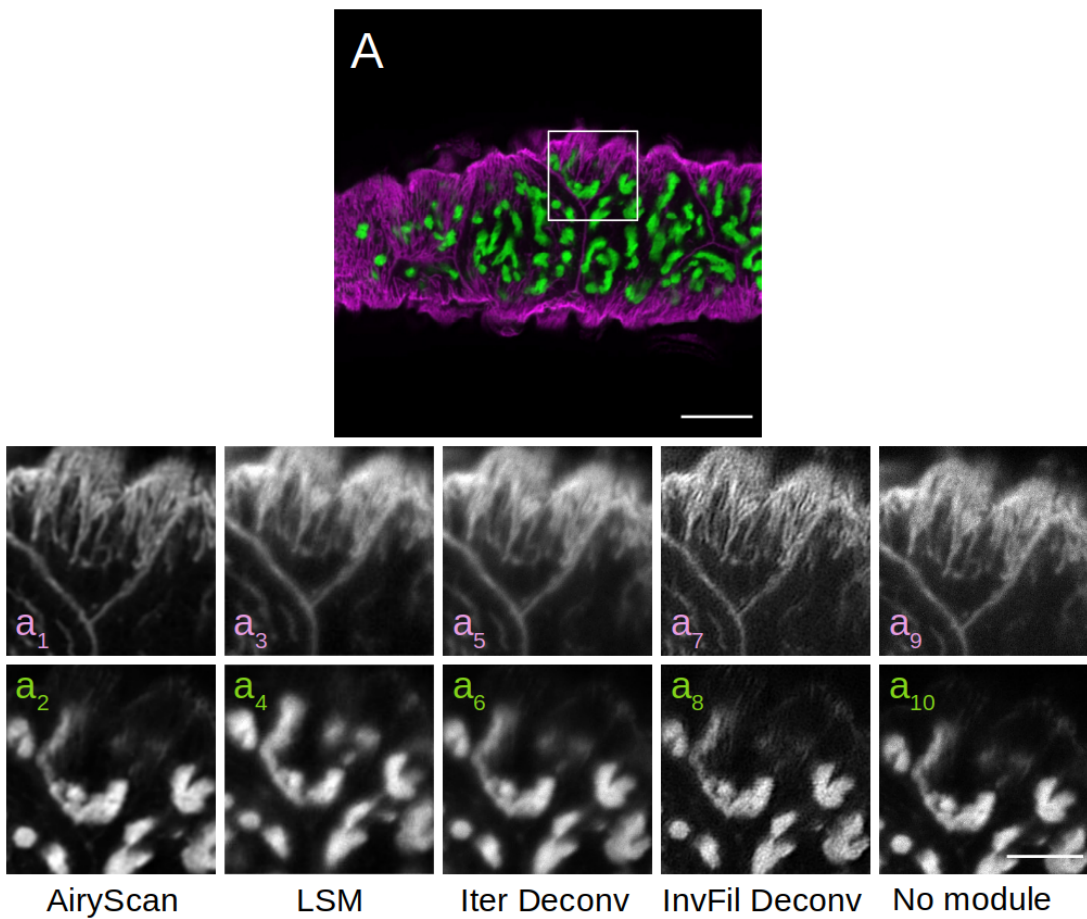


Figure 6.3.1: A: Airyscan of a blowfly salivary gland, white square marks the magnified area. All images are shown at an approximately similar optical section of a z-stack. Top row (odd index) is the basolateral membrane labelled by anti-mouse-AlexaFluor568, bottom row (even index) is Actin, labelled by AlexaFluor488-Phalloidin. Objective lens: $40\times/1.2$ lmm glycerin immersion. Scalebar on original image is $10\ \mu\text{m}$, on the zoomed in image is $5\ \mu\text{m}$.

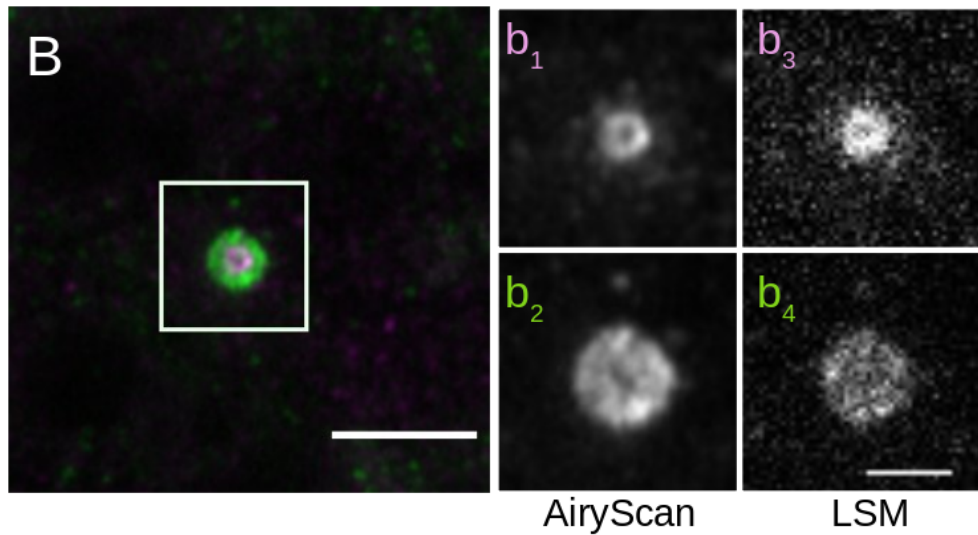


Figure 6.3.2: B: Airyscan of AX2, white square marks the magnified area. All images are shown at an approximately similar optical section of a z-stack. Top row (odd index) is CP91 labelled by AlexaFluor568, bottom row (even index) is CP224 labelled by AlexaFluor488. Objective lens: $63\times/1.3$ Oil immersion. Scalebar on original image is $10\ \mu\text{m}$, on the zoomed in image is $1\ \mu\text{m}$.

7 | DECONVOLUTION

7.1 INTRODUCTION

AIM To obtain/restore high resolution images using deconvolution methods.

High resolution microscopy is often plagued by blurriness due to diffractions (convolution). Inverse convolution (deconvolution) methods can be performed to obtain convolution-free images by describing a mathematical function called the Point Spread Function (PSF) to recalculate diffracted light, stray light, and out-of-focus light back to its origin [18].

7.2 METHODS

Two samples, 200 nm Tetraspeck beads and *Dictyostelium discoideum* cells (AX2 line) were used in this experiment. Deconvolution was performed using three methods; (constrained) iterative, fast iterative, and (regularized) inverse filter, each obtained by calculation of PSF from direct measurement in the experiment (measured/M) and through calculation from the parameters of the device (theoretical/T). To obtain the FWHM, a line profile measurement was done for each beads, for each channels. Afterwards procedures for gaussian fit and averaging were done in Python (script available publicly on [GitHub](#), or by request).

7.3 RESULTS AND DISCUSSION

7.3.1 Tetraspeck beads

The 200 nm Tetraspeck beads emit at four different wavelengths: 430 nm (blue), 515 nm (green), 580 nm (orange) and 680 nm (dark red) [19], these correspond to Ch₃, Ch₂, Ch₁, and Ch₄ in the case of this experiment. The beads were imaged as depicted in Fig. 7.3.1. During the experiment, only three good beads that could be found. From the raw (input) image, a PSF was calculated (measured PSF). The PSF obtained in this way was then used for deconvolution purposes. Another PSF was calculated (theoretically) from various imaging parameters/device parameters and also used for deconvolution procedures (theoretical PSF) as a comparison.

At first glance, it can be observed the various deconvolution methods (iterative, fast iterative, and inverse filter) performed differently, especially in the z-dimension. It can also be noticed that there is a different focus of the different channels, most prominently seen, again, in the z-dimension. The shift could be caused by chromatic abberations. This shift in focus that can be seen on all images could also be caused by movement of the filter carousel when changing measurement channel during imaging that does not retain the same original focus. Another immediate observation

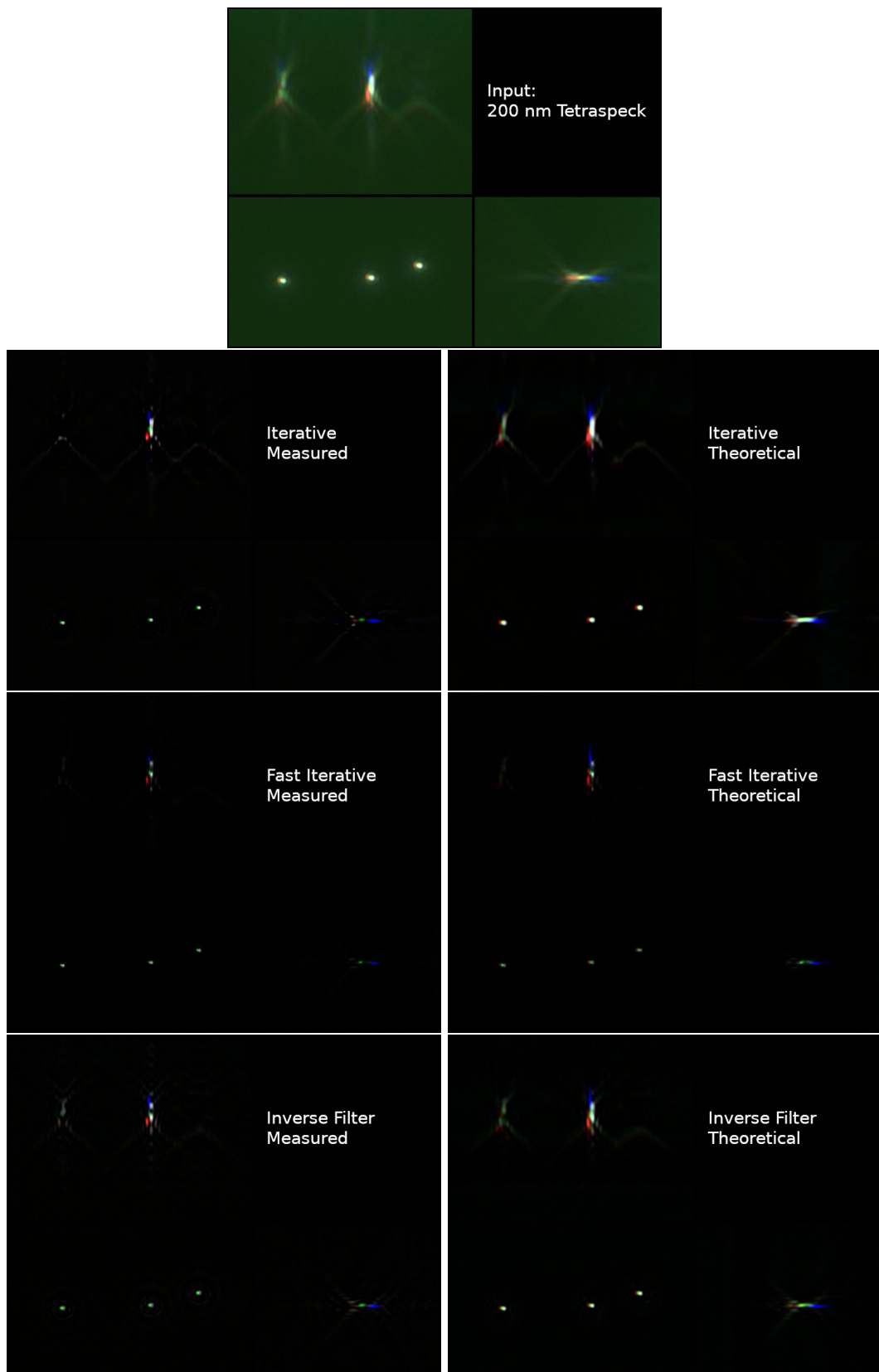


Figure 7.3.1: Orthoview of tetraspeck beads acquired raw (called input) and deconvoluted on 4 channels: red/orange, green, blue, and infrared/dark red. Objective lens: Plan Apochromat 100 \times /1.4 Oil Ph3

shows that the green channel exhibit a relatively rough background noise which is typical (not shown).

Comparing the measured deconvolutions and the theoretical ones, it is immediately obvious that the resolution in the z-dimension of the measured is better than the theoretical. Calculating the FWHM of each deconvolution methods would give a better overview of their performance in the xy-dimension. This is done by taking a line profile (intensity profile) of all acquired beads on all channels, then make a gaussian fit of the intensity profile and calculate the average FWHM. In principal, the resolution in z-dimension can also be obtained in a similar way, however the difference would seem that in this dimension, the object would be in a different shape (more elongated), and also consequently the intensity profile should be taken along the z-axis.

The gaussian fits were first performed using an offset parameter due to the presence of measurements that seems to be off the baseline (channel 2 of the input image). However this seems to set the gaussian fit to fail on some other measurements. Adjusting the initial guess of this parameter (and also the others: A, μ , and σ) seems to remedy the failure on these measurements, however it would then arbitrarily cause failure on completely different measurements. Since no pattern or explanation could be obtained, it was then decided to make a baseline correction to the initially problematic measurements, namely channel 2 of the input image by subtracting the intensity values with the minimum value which provides the baseline of around 0, putting them on the same baseline level as the other measurements. This allows for the removal of the offset term of the fit and resulted in the successful application of the whole fitting procedure. It is probably also worth mentioning that no intensity normalization was conducted due to the fact that the fit at this point seems fine already.

The result of this is given in Tab. 1 and visualized in a barplot in Fig. 7.3.2. It can be seen here, that the FWHM of the input image is naturally the largest, due to the fact that no deconvolution procedure was performed. The FWHM of the input image is around 30% larger than the actual size of the beads (200 nm), and all attempts of the deconvolution procedures managed to bring the FWHM lower. It can be concluded that all methods using measured PSF consistently performs better on all channels than methods using theoretical PSF except in the case of measurement of fast iterative method on channel 4 where the values are really close. And among the three deconvolution methods, fast iterative constantly yields the smallest FWHM on all channels.

Table 1: FWHM⁺ for Tetraspeck beads

| | Input | Inverse Filter (T) | Inverse Filter (M) | Iterative (T) | Iterative (M) | Fast Iterative (T) | Fast Iterative (M) |
|-----|--------------|--------------------|--------------------|---------------|---------------|--------------------|--------------------|
| Ch1 | 347.10(6.18) | 231.22(1.81) | 214.64(1.12) | 290.29(0.15) | 230.56(2.12) | 188.48(9.44) | 149.50(2.50) |
| Ch2 | 301.83(2.90) | 226.78(1.65) | 209.23(4.25) | 246.10(2.32) | 198.97(2.90) | 182.06(19.87) | 145.06(13.58) |
| Ch3 | 334.31(4.84) | 206.58(1.67) | 183.41(1.32) | 282.08(2.94) | 211.90(4.84) | 171.34(3.06) | 127.85(2.56) |
| Ch4 | 388.33(3.65) | 245.41(0.87) | 228.45(2.97) | 300.79(0.95) | 212.87(3.65) | 184.99(4.76) | 185.11(4.69) |

⁺Given in nm (average of the three present beads), standard deviation in parenthesis. (M) means the PSF is acquired by measurement, and (T) means the PSF is acquired by theoretical calculations of imaging parameters. Ch1 is red/orange (580 nm), Ch2 green (515 nm), Ch3 is blue (430 nm), and Ch4 is infrared/dark red (680 nm).

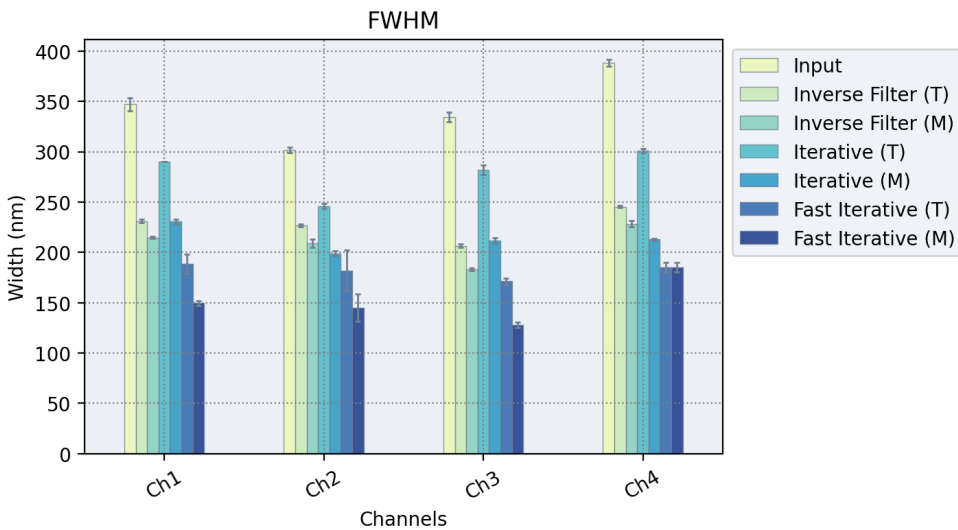


Figure 7.3.2: FWHM of Tab. 1 in barplot with the standard deviation given as error bars.

The optical resolution following the Rayleigh criterion, given by $d = 0.61 \times (\lambda/NA)$, where d is the minimum distance where two points are resolved, λ is the wavelength of illumination, and NA is the numerical aperture of the lens, yield for each channel 1-4 (i.e. red/orange, green, blue, and dark red/infrared): 252.71 nm, 224.39 nm, 187.35 nm, and 296.28 nm respectively. Given that the minimum distance for two points to be considered resolved is where the maximum of one point is directly on the first minimum of the other peak (\approx FWHM), it seems that at least in the xy-dimension, the calculated FWHM of all deconvolution methods at all considered channels does not correspond all that well with the Rayleigh criterion.

Although in principal, it is known that the iterative method should give the best resulting image quality because of its ability to calculate light from various focal planes back to its place of origin, with the disadvantage being that it may take a long time for this deconvolution method to be performed due to the number of iterations in performing deconvolution algorithm (40 in this case). The fast iterative method is basically the same with the limitation on the number of iterations. The inverse filter is a method that involves a Fourier transformation and is the fastest method among these three.

7.3.2 AX2 cells

The PSF obtained from previous experiment on tetraspeck beads was then used for the deconvolution of AX2 cells images. Shown in Fig. 7.3.3 (Left). The following organelles are labelled: nucleus by DAPI, CP91 (core of centrosome) by anti-rabbit-AlexaFluor568, and CP224 (corona of centrosome) by anti-mouse-AlexaFluor488.

A montage image of each organelle according to the deconvolution methods is shown in Fig. 7.3.3 (Right). It can be seen that most deconvolution methods bring better image results in comparison to the raw/input image where contrasts are improved and structures are more readily recognizable. The size of CP91 is shown to be the smallest for the fast iterative method in comparison to other methods. This is consistent with the result from the discussion above where this deconvolution method yields the smallest FWHM.

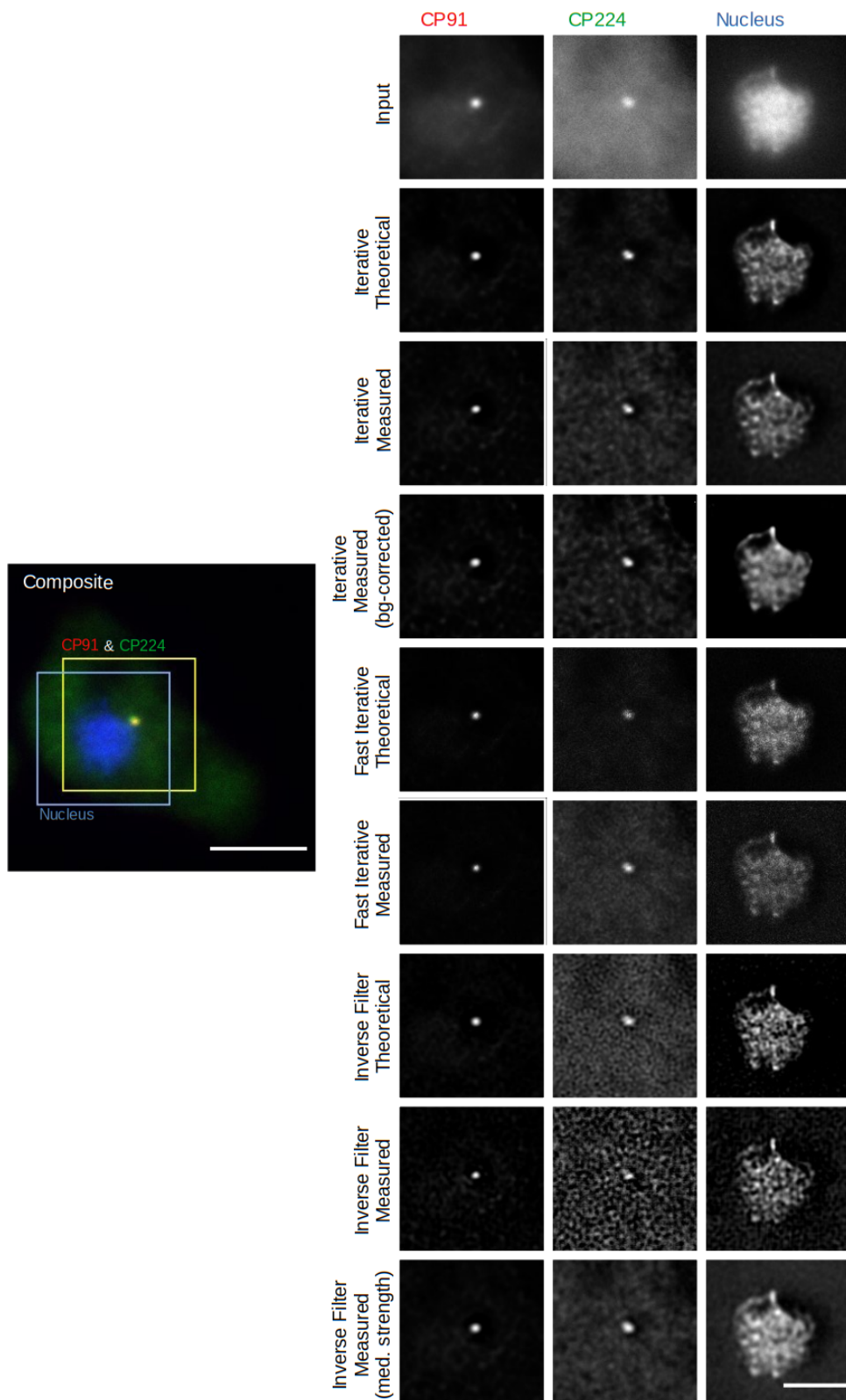


Figure 7.3.3: Objective lens: Plan Apochromat 100 \times /1.4 Oil Ph3. **Left:** The composite of single representative optical sections of a z-stack of the raw input image of AX2 cells. CP91 is labelled by AlexaFluor-568 (red), CP224 by AlexaFluor-488 (green), and the nucleus by DAPI (blue). Gamma correction of 1.50 was applied on all channels of the composite for visualization purposes. Yellow square marks the cropped area on CP91 and CP224 channel on the right montage, blue square marks the cropped area on the nucleus channel. Scale bar is 5 μm . **Right:** A montage of the resulting deconvolution process. Each image shown here corresponds to the optical section shown on left image. No gamma correction. Scale bar is 3 μm .

The iterative method with measured PSF produces a good CP224 images along with the vague fluorescence signals of AlexaFluor-488 bound to the + ends of the microtubules. This feature can also be observed with the fast iterative method using measured PSF, though very vague, and seems absent in the method using theoretical PSF for both iterative and fast iterative. The inverse filter method seem to produce a mottling artifact in this channel. A mottling artifact is a phenomenon where signals, particularly noise in the background gets amplified by deconvolution algorithms. This phenomenon occurs usually with inversion algorithms, but iterative algorithms are also not free from this [20].

Inspecting the DAPI channel, it can be easily seen that the fast iterative method produces a much grainier image in comparison to the iterative method, both for the theoretical and measured PSF. This occurs on both previous channels of this method as well, just more prominently displayed here. This can be attributed to the limited number of iterations used in this method in comparison to the iterative method. The resulting images from the inverse filter method show, again, an artifact, which is arguably a ringing artifact. This artifact has an appearance of dark ripples around bright features of an image [20].

As a comparison, another set of images were also acquired for the iterative method using measured PSF, however this time using background correction. This acquisition shows a better form of the nucleus in the DAPI channel but does not seem to introduce major improvements for the other two channels in this observation. Another voluntary acquisition was also conducted for the inverse filter method using measured PSF. This time the artifacts appear less prominent and the images look more appropriate.

For the most part, the ability of the methods employed to restore images has a lot to do with the PSF itself and the raw image being restored, in regards that the PSF that is used should match the corresponding image. If there are aberrations in the image, then the PSF should also contain a corresponding aberrations as well. Otherwise, the deconvolved image may contain errors or be poorly restored [20]. Managing appropriate settings during image acquisitions also plays a major role.

8

CA-IMAGING

8.1 INTRODUCTION

AIM To obtain/depict changes in Calcium concentration of a blowfly salivary gland upon stimulation by serotonin.

The blowfly salivary glands provide an ideal object for studying stimulus-dependent spatiotemporal intra- and intercellular Ca^{2+} dynamics in an intact 'mini-organ', since its tubular secretory region is easily accessible to experimental manipulation and Ca^{2+} -imaging experiments. The secretory portion of the gland consists of a single layer of uniformly differentiated epithelial cells that are grouped around a central lumen [21]. The membrane of a blowfly's salivary gland is covered by ion pumps. Due to the deep infoldings (canalliculi) of the apical membrane, there is a huge amount of ion pumps. These infoldings enlarges the apical membrane up to 250 times in comparison to a flat membrane. Normally, after dissection, the salivary gland produces almost no saliva. However, the presence of serotonin (5-HT) induces salivation. Serotonin itself has 2 different receptors on the plasma membrane.

The detection of Ca^{2+} utilizes the fluorescent dye fura 2 whose fluorescence emission is independent of Ca, but its excitation changes depending on $[\text{Ca}^{2+}]$. Fig. 8.1.1 describes the excitation response of fura 2 due to Ca ions. The excitation maximum at nominally free Ca condition is at 365 nm (isosbestic point). However, at high concentration of Ca, the excitation maximum sits at 340 nm. In contrast, the excitation at 380 nm decreases.

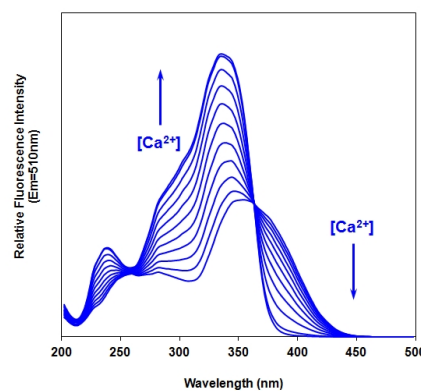


Figure 8.1.1: Excitation spectrum of fura 2 fluorescent dye in the presence of Calcium. Image source: <https://www.aatbio.com/products/fura-2-am-ultrapure-grade-cas-108964-32-5>. Accessed: 09/12/2020.

Since fluorescence intensity depends on the concentration of fluorophores, which in turn depends on cell conditions (bleaching, unequal distributions, volume changes, etc), measuring both excitation wavelength allows the elimination of these influencing factors and the signal then depends only on the concentration of calcium.

8.2 METHODS

The specimen is a dissected abdominal part of the salivary gland of *Calliphora vicina*. The specimen is then loaded with the modified fluorescent dye fura 2.

The imaging is conducted using an inverted microscope equipped with Fluar $20\times/0.75$ NA, a fluorite optic with high transmission for UV light. The sample is then excited at 340 ± 5 nm and 380 ± 5 nm. Emission is filtered using a bandpass at 510 ± 42 nm. The light source is a Xenon arc lamp that emits a white light with an even spectrum in the UV range. Wavelength selection for excitation is performed by a grating monochromator that passes a select wavelength through a slit.

The gland was tested with different Serotonin (5-HT) concentrations (1, 3, and 10 nM). The reagents are listed in Table 2 along with the order and time of addition.

Table 2: List of reagents

| Reagent | Addition time |
|-------------------------|---------------|
| Ringer | start |
| 1 nM 5-HT | 1 min |
| 3 nM 5-HT | 4 min |
| 10 nM 5-HT | 9 min |
| Normalringer | 13 min |
| 20 nM MnCl ₂ | 16 min |

At the end of the measurement, MnCl₂ is added to quench the remaining fluorescence from Ca binded fura 2 and allows the requisition of autofluorescence from the sample itself. Subtracting all the acquired measurement results by this background signal gives the actual fluorescence signal due to Ca.

8.3 RESULTS AND DISCUSSION

Observing the measurement result in Fig. 8.3.1A, it can be seen that there is an oscillation in the fluorescence signal obtained by stimulation of 5-HT under the concentration of 10 nM. This oscillation that is evident on one excitation spectrum (e.g. 340 nm) is mirrored on the other excitation spectrum (380 nm). The fluorescence oscillation increased even more after the addition of 10 nM 5-HT, which however in this experiment seemed like a plateau, the frequency increase can only be observed minimally. Then afterwards the fluorescence signal decreases after quenching.

Indicators are charged molecules and do not easily pass lipid membranes. To promote the introduction of fluorescent indicators into the interior of single cells or tissue, the method that can be used is adding lipophilic groups (acetoxymethyl or acetate ester groups) to the charged indicator molecule. The indicator complex becomes neutral and lipophilic and hence membrane-permeant. Once the complex has entered into the cytosol, cytoplasmic esterases gradually cut off the lipophilic groups and the free indicator molecule is then trapped in the cytosol and ready to bind with Ca²⁺ [22]. However, if the concentration of fura 2 is too high, then there is the danger of influencing the physiology of the cell by the increase in concentration of the cut-off lipophilic groups (acetic acid and formaldehyde).

The use of fura 2, a ratioing dye, in principle allows the quantitative determination of [Ca²⁺]. This follows the Grynkiewicz equation (1).

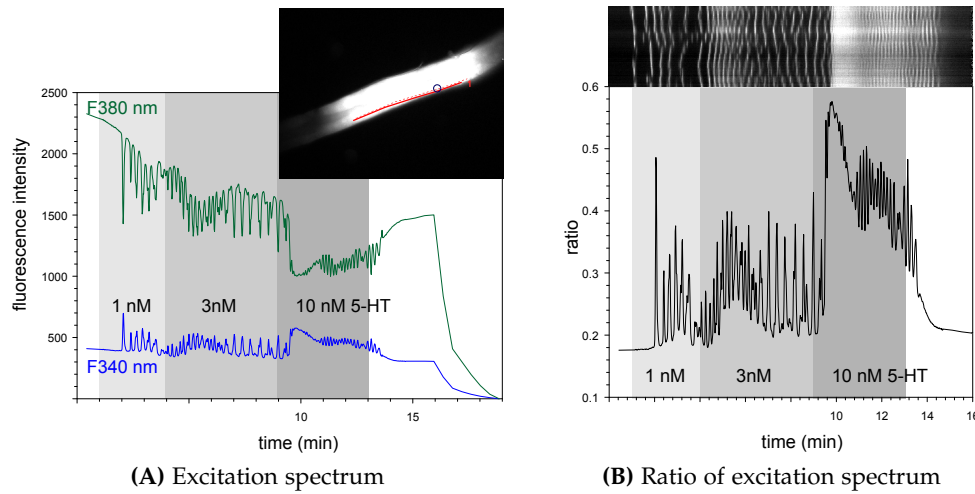


Figure 8.3.1: Measurement results. **A** is the measurement result of the excitation spectra at 340 and 380 nm over time, inset is the selected region of interest on the specimen (red line with width 1 pixel.). **B** is ratio of the obtained spectra over time, inset is the space-time plot of calcium concentration. The addition of serotonin (5-HT) is marked on both figures accordingly.

$$[\text{Ca}^{2+}] = K_d \times b \times \frac{R - R_{\min}}{R_{\max} - R} = K_d^* \times \frac{R - R_{\min}}{R_{\max} - R} \quad (1)$$

K_d is the dissociation constant of Ca, b is the instrument factor, R_{\max} is R at high $[\text{Ca}^{2+}]$ (or saturating conditions), R_{\min} is R at $[\text{Ca}^{2+}] = 0$, R is the ratio of the measured fluorescence intensities, K_d^* is the combination of b and K_d . The constant b along with R_{\min} and R_{\max} can be obtained by calibration. However the quantitative determination of $[\text{Ca}^{2+}]$ was not performed in this experiment.

The red line in the inset of Fig. 8.3.1A shows the part where the fluorescence measurement was conducted. The obtained fluorescence ratio is presented in Fig. 8.3.1B. Here it can also be seen that by the addition of 1 nM 5-HT, oscillations can be observed. Oscillations of $[\text{Ca}^{2+}]$ in response to intermediate agonist concentrations have been observed in many different cell. In the majority of non-excitable cells investigated so far, these oscillations are believed to be based on a periodic release of Ca^{2+} from intracellular stores [21]. Ca^{2+} in this experiment also exist extracellularly due to the Ringer solution which contains CaCl_2 . The oscillation frequency increases by adding a higher concentration of Ca^{2+} (5 nM). A jump in signal then occurred after the addition of 10 nM 5-HT with an even higher frequency of oscillation. This fluorescence signal behaviour also coincides with the space-time plot provided as inset.

From Fig. 8.3.1B, it can be conclusively seen that serotonin (5-HT) induces the transport of Ca^{2+} in blowfly salivary gland, which normally does not produce saliva after dissection. The concentration of Ca^{2+} in blowfly salivary gland is responsive towards the amount of 5-HT that is added.

9

FLUORESCENCE CORRELATION SPECTROSCOPY

9.1 INTRODUCTION

AIM To distinguish cell morphologies during cell cycle through the detection of ribosomes.

Fluorescence Correlation Spectroscopy (FCS) is based on the detection of fluorescence signal from a very small volume. It is a technique that allows one to measure concentrations and diffusion coefficients of fluorescently labelled molecules. In this experiment, confocal microscopy (LSM) is coupled with FCS to estimate calibration parameters and convert fluorescence intensities to the concentration (of the corresponding protein of interest) in living cells [23].

9.2 METHODS

Data acquisition was performed as the following:

- Calibration of the observation volume using AlexaFluor488 (as EGFP analog - Enhanced GFP), in FCS acquisition mode, to determine the size of the observation volume (*in vitro*).
- Calibration of the image intensities (LSM imaging) against concentration (FCS) using monomeric EGFP expressed in yeast (*in vivo*).
- Determination of fluorescence probability through FCS of dimeric EGFP expressed in yeast (*in vivo*).
- Z-stack acquisition of protein of interest.

9.3 RESULTS AND DISCUSSION

9.3.1 Rpl3

Proteins in yeast in this experiment are genetically expressing GFP. The protein is Rpl3, a Ribosomal 60S subunit protein L3, it is homologous to mammalian and bacterial ribosomal protein L3 [24]. The measurement of the fluorescence intensity of GFP in a yeast cell is proportional to the number of ribosomes contained within it.

9.3.2 FCS

The detectors in a modern LSM system are able to show a linear dependency of fluorophore concentrations and its intensities within several orders of magnitude [23].

In order to be able to quantify and convert the relative fluorescent intensities to physical quantities (i.e. the amount of fluorescently labelled proteins) a calibration of the dependency has to first be established. To this aim, FCS can be used.

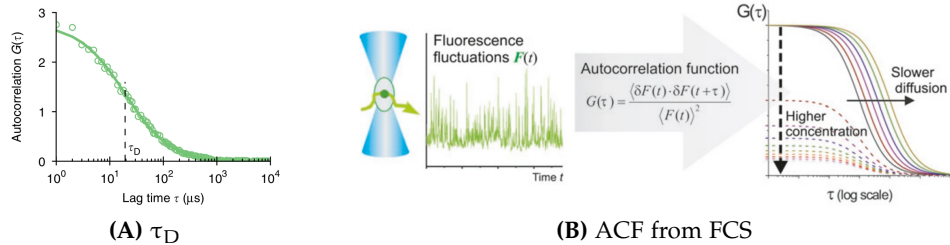


Figure 9.3.1: A: Obtaining τ_D from ACF (taken from Politi et al [23]). B: Obtaining the ACF from FCS measurement (taken from Bacia et al [25]).

OBSERVATION VOLUME In FCS fluorescence intensity is measured at a certain location of a sample. The intensity in that observation volume fluctuates with time because there is a flux of fluorescent molecules traversing the observation volume. The size of the observation volume is given by

$$V_{\text{eff}} = \pi^{\frac{3}{2}} w_0^2 z_0 \quad (2)$$

with $w_0 = \sqrt{2(D_{\text{dye}} \tau_D)}$, $z_0 = \kappa w_0$, and $\kappa = \frac{2.33 n}{NA}$, where w_0 and z_0 describes the dimension of the observation volume, n is the refractive index, NA is the numerical aperture, D_{dye} is the diffusion coefficient, and τ_D is the average diffusion time. The latter is obtained by fitting the Auto Correlation Function (ACF) to a physical model of diffusion (Fig 9.3.1A) while the other quantities are already known either as experimental parameters (n and NA) or as an already established value as in the case of D_{dye} of EGFP.

The ACF is a correlation of a fluorescence signal with a delayed copy of itself as a function of delay. It is the result of the FCS measurement as illustrated in Fig. 9.3.1B.

FLUORESCENCE PROBABILITY Fluorescence measurements assumes that the amount of fluorescence being detected is proportional to the number of fluorescent molecules present. However fluorescent molecules can undergo many different processes that induces non-fluorescent states [26]. This introduces a challenge in interpreting the outcome of such fluorescence measurements where possibly not all molecules emit a fluorescence signal.

A simple quantity, fluorescence probability, depicts the proportion of molecules that emit fluorescence and it is given by

$$p_f = \frac{B_{\text{dimer}}}{B_{\text{monomer}}} - 1 \quad (3)$$

The fluorescence probability reflects to which degree that a fluorescent species are not fluorescently active, i.e. do not emit a signal at all. This is obtained through the calculation of a quantity called the brightness (B) of a monomeric and dimeric fluorescent species.

The brightness is given by

$$B = \frac{I}{N} \quad (4)$$

where I is the fluorescence intensity and N the number of fluorescent molecules. This relates to the y-intercept of the ACF fit (see Fig. 9.3.2), or the ACF at time = 0 ($G(\tau)$ at $\tau = 0$).

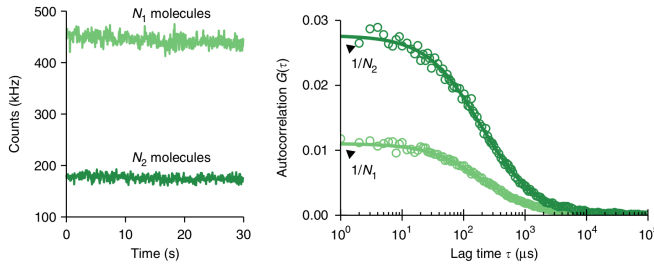


Figure 9.3.2: Relationship between N and ACF fit (taken from Politi et al [23])

CORRECTIONS Due to the fact that fluorescent species are susceptible to bleedings during fluorescent measurements, correction of the obtained relating to this has to be performed. The correction is done through the ratio of the initial fluorescence intensity (I_0) and the fluorescence intensity of the measurement itself (I) as given by

$$N_{\text{corr}} = \frac{I_0}{I} N . \quad (5)$$

The usual background correction is also necessary to be performed alongside this.

CONCENTRATION Taking those factors above into account, then the concentration of the fluorescent molecules can be calculated as follows:

$$C = \frac{N_{\text{corr}}}{N_A V_{\text{eff}}} \quad (6)$$

where N_A is Avogadro's constant.

9.3.3 LSM

After establishing the necessary parameters from FCS, imaging of the protein of interest (POI) in yeast was done by acquiring a z-stack through LSM. The alignment of pixel positions of the observation volume in the FCS measurements and the LSM image acquisitions were done automatically by the employed MATLAB software.

Since in LSM the images are acquired in photon counting mode, quantities such as the brightness (or correspondingly, the intensity as well) of FCS acquisitions have to be transformed to kHz according to the corresponding measurement dwell time (in FCS).

$$B (\text{kHz}) = \frac{\langle B \rangle}{(\text{dwell time})_{\text{FCS}}} \quad (7)$$

CALIBRATION The obtained concentration of the fluorescent molecules (or the POI) from FCS measurement can be calibrated with the fluorescence intensity obtained through LSM acquisition to yield a plot as exemplified in Fig. 9.3.4.

CONCENTRATION With the slope obtained by the calibration, the concentration of the POI can be calculated using the fluorescence intensity of a voxel by

$$[C] = \frac{I_{\text{voxel}}}{\text{slope}} \quad (8)$$

where the intensity of a voxel in the frequency form is

$$I_{\text{voxel}} = \frac{\sum_{j=1}^J I_j}{N_{\text{voxel}}} \quad (9)$$

with the measurement dwell time now is from the LSM acquisition. The number of voxel is the total area of each layer in a z-stack divided by the size/area of a pixel such as

$$N_{\text{voxel}} = \frac{\text{Area}}{\text{Pixel Area}} \quad (10)$$

AMOUNT OF PROTEINS The Rpl3 protein is located in the ribosomes of yeasts and the amount of which can now be calculated according to

$$N_{\text{ribosome}} = [C] \cdot \text{pixel size} \cdot z_{\text{step}} \cdot N_A \cdot N_{\text{voxel}} \quad (11)$$

And finally, correcting the amount of ribosome to the fluorescence probability would then yield

$$N_{\text{ribosome}} = \frac{N_{\text{ribosome}}}{p_f}. \quad (12)$$

A widefield acquisitions was performed alongside the LSM acquisitions to aid the determination of the cell cycle phase (G1/S/G2/mitosis) of the yeast cells (Mother-Bud cells). This determination was done manually as illustrated in Fig. 9.3.3.

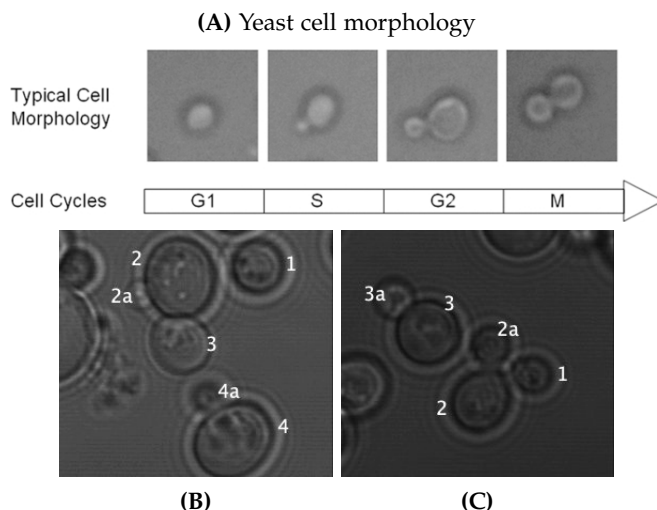


Figure 9.3.3: A: Illustration of yeast cell morphology through cell cycle progression [27]. B and C are examples of widefield acquisition of yeast cells in the experiment showing the identification and numbering of mother and bud cells in different cell cycle.

Providing that the experimental (pixel) dwell time in LSM is $12.6 \mu\text{s}$, dwell time in FCS is $1.53 \mu\text{s}$, pixel size is 72 nm (pixel area = 72^2 nm^2), and the z-step is 460 nm , calculations and calibrations can be done according to the above mentioned explanations.

Assuming a gaussian shaped illuminated volume, the confocal/observation volume in this experiment is $0.672 \mu\text{m}^3$ as obtained by Eq. 2 ($\kappa = 7.1$) from the FCS measurement of different concentrations of monomeric AlexaFluor488 (henceforth addressed as EGFP) in solutions (*in vitro*). The result of this measurement is then compared to the calibration of FCS measurement of monomeric EGFP expressed in yeast cells (*in vivo*) to its fluorescence intensity from LSM, shown in Fig. 9.3.4.

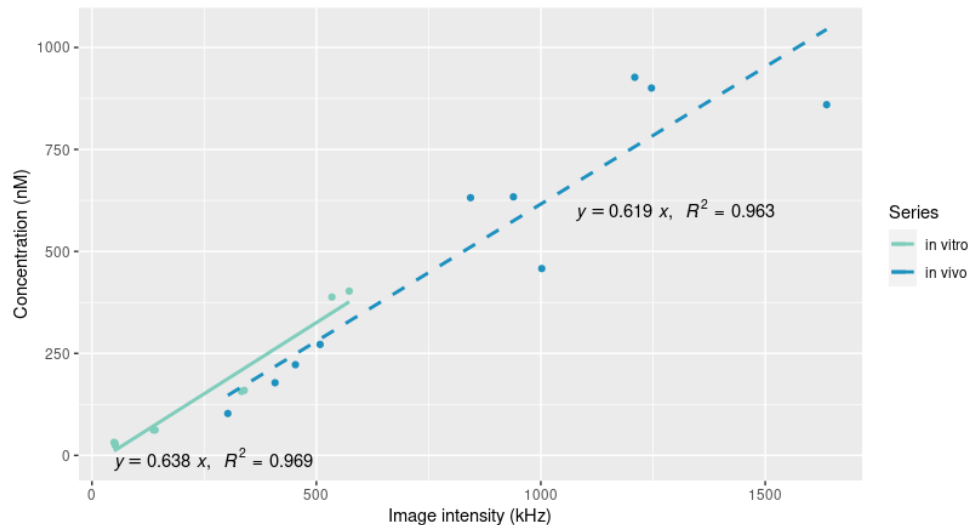


Figure 9.3.4: Calibration plot of concentrations against the intensity of monomeric EGFP in solution (*in vitro* - cyan solid line) and yeast expressing monomeric EGFP (*in vivo*). The concentration for *in vitro* (blue dashed line) measurement is obtained from calculation of FCS measurements while *in vivo* from LSM. Both linear fits are set at 0 intercept.

As can be seen from both of these calibration plots, the slopes yielded by both methods (*in vitro* and *in vivo*) are rather similar even though the calibration of the monomeric EGFP in solutions was done without using information from LSM acquisitions (slope ~ 0.6). This indicates initially that the slope obtained from both of this methods can be used in the determination of the amount or concentration of the POI. However, values of B are in a whole different magnitude (median *in vitro*: 4.70371, *in vivo*: 0.00335), where the brightness of EGFP in solution is higher than in cells/yeast. This means that the information obtained from the *in vitro* measurements may not be necessarily utilizable especially when it concerns to calculating the p_f where the value of brightness matters a lot.

Following Eq. 3, the resulting fluorescence probability is 0.46. As mentioned, this value is used to correct the amount of calculated ribosome and is especially important to consider, because without it the resulting amount would be underestimated.

The plot of N_{ribosome} against the volume of each mother and bud cells (Fig. 9.3.5A) demonstrates a positive, strong, and significant correlation ($\text{corr} = 0.95$). Which means that the N_{ribosome} is not a constant value as previously believed, on the contrary, it is the density that is relatively constant ($5000\text{-}8000 \text{ counts}/\mu\text{m}^3$). This means that considering cells have different sizes, the number of ribosomes can not be used to indicate a cell's state in the progression as demonstrated by the fact that a higher

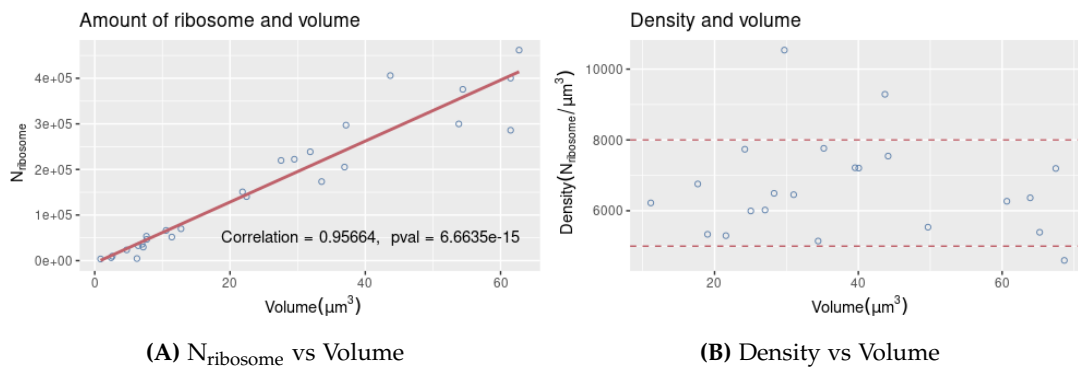


Figure 9.3.5: A: correlation plot of N_{ribosome} against volume of individual mother and bud cells. B: plot of density against volume of whole cells (sum of mother + bud cells). Red dashed lines in B are only for illustrative purposes.

amount of N_{ribosome} corresponds to larger cells (constant density). This is shown in Fig. 9.3.5B where the density varies rather constantly within the band as indicated by the (arbitrary) dashed line.

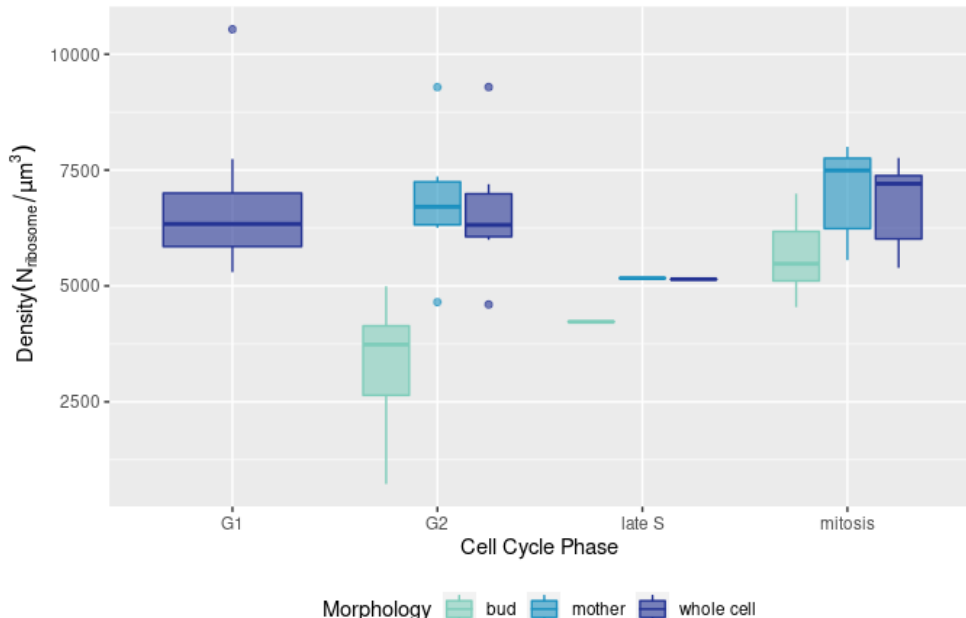


Figure 9.3.6: Boxplot of density of different cell morphologies across the cell cycle. Whole cells in the G₂, late S, and mitosis is the sum density of mother and bud cells in these phases.

The inability of this to distinguish cell morphology during cell cycle progression, or rather the constant value of density, is visualized by the boxplot in Fig. 9.3.6 which shows that the density does not exhibit any meaningful change during the course of the cell cycle. The statistical test of which is supplied at the end of this chapter. In this case the late S phase is excluded from analysis due to insufficient amount of observation. The analysis by ANOVA for three cell cycle phases indicates no significant difference, hence not carried on further to test the individual differences by pairwise t-tests.

On the single cell level, however, discrimination between mother and bud cells is possible to be done with this technique by using the density as a measure. Separating

the data shows that buds constantly exhibit a lower density in comparison to mother cells during the cycle from G₂ up to mitosis (Fig. 9.3.6). Evidence to this is further supported by statistical tests that found significant difference (by ANOVA for two groups: buds and mothers) between the density of buds and mother cells across the whole cell cycle progression (also supplied at the end of this chapter). Since only two groups was tested, no pairwise t-test was necessary.

Additional analysis was also done on the subset of buds. From the acquired data of this experiment, providing that singular observation is removed, it seems that even buds can be distinguished by the density according to which cell cycle phase they are currently in. The evidence is again supplied by the end of this chapter where ANOVA was carried on for two groups of cell cycle phase (G₂ and mitosis) with result showing significant difference.

FCS Test Report

Howard Setyamukti

Data Summary

Aggregated data, termed as whole cells (mother+buds), exclude S phase due to only 1 observation.

```
summary(rpl)

##  CellCyclePhase      Morphology      Density
##  G1      :8      whole cell:21   Min.    : 4598
##  G2      :6                  1st Qu.: 5994
##  mitosis:7                 Median  : 6454
##                               Mean    : 6725
##                               3rd Qu.: 7215
##                               Max.    :10537
```

ANOVA

The following is the result of ANOVA where it is demonstrated that there is no significant difference between groups.

```
res.aov <- aov(Density ~ CellCyclePhase, data = rpl)
summary(res.aov)
```

```
##             Df  Sum Sq Mean Sq F value Pr(>F)
## CellCyclePhase 2 108063  54031  0.026  0.975
## Residuals     18 37902777 2105710
```

Validity Check

Normality test, confirmed by Shapiro-Wilk test of normality.

```
#plot(res.aov, 2)
aov_residuals <- residuals(object = res.aov)
shapiro.test(x = aov_residuals)
```

```
##
##  Shapiro-Wilk normality test
##
## data: aov_residuals
## W = 0.91632, p-value = 0.07326
```

FCS Test Report

Howard Setyamukti

Data Summary

Separated data, termed as mother and bud, exclude G1 phase.

```
summary(rpl)
```

```
##   CellCyclePhase Morphology    Density
##   G2      :11      bud     :13  Min.   : 727.9
##   late S : 2      mother:14  1st Qu.:4822.2
##   mitosis:14          Median :5571.6
##                               Mean   :5748.8
##                               3rd Qu.:6947.2
##                               Max.   :9289.5
```

ANOVA

The following is the result of ANOVA where it is demonstrated that there is significant difference between groups (mothers and buds).

```
res.aov <- aov(Density ~ Morphology, data = rpl)
summary(res.aov)
```

```
##             Df  Sum Sq Mean Sq F value    Pr(>F)
## Morphology     1 32032821 32032821    15.07 0.000671 ***
## Residuals    25 53153829  2126153
## ---
## Signif. codes:  0 '***' 0.001 '**' 0.01 '*' 0.05 '.' 0.1 ' ' 1
```

Validity Check

Normality test, confirmed by Shapiro-Wilk test of normality.

```
#plot(res.aov, 2)
aov_residuals <- residuals(object = res.aov)
shapiro.test(x = aov_residuals)
```

```
##
##  Shapiro-Wilk normality test
##
## data: aov_residuals
## W = 0.97152, p-value = 0.6423
```

FCS Test Report

Howard Setyamukti

Data Summary

Only buds data, exclude S phase due to only 1 observation.

```
summary(rpl)
```

```
##  CellCyclePhase Morphology      Density
##  G2      :5      bud:12      Min.   : 727.9
##  mitosis:7                      1st Qu.:4037.2
##                                         Median :5043.6
##                                         Mean   :4651.1
##                                         3rd Qu.:5624.6
##                                         Max.   :6990.6
```

ANOVA

The following is the result of ANOVA where it is demonstrated that there is significant difference between groups (buds at different cell cycles).

```
res.aov <- aov(Density ~ CellCyclePhase, data = rpl)
summary(res.aov)

##             Df  Sum Sq  Mean Sq F value Pr(>F)
## CellCyclePhase  1 16892448 16892448   11.26 0.0073 **
## Residuals     10 15005037 1500504
## ---
## Signif. codes:  0 '***' 0.001 '**' 0.01 '*' 0.05 '.' 0.1 ' ' 1
```

Validity Check

Normality test, confirmed by Shapiro-Wilk test of normality.

```
#plot(res.aov, 2)
aov_residuals <- residuals(object = res.aov)
shapiro.test(x = aov_residuals)
```

```
##
##  Shapiro-Wilk normality test
##
##  data:  aov_residuals
##  W = 0.96273, p-value = 0.822
```

10

FLUORESCENCE RECOVERY AFTER PHOTOBLEACHING

10.1 INTRODUCTION

AIM To investigate the dynamics of two different proteins (NE81 and Erg24) after photobleaching.

In this experiment, Fluorescence Recovery After Photobleaching (FRAP) method is utilized to investigate the dynamics of proteins in a living cell. Photobleaching refers to the fact that fluorescently tagged proteins are bleached by high intensity laser on certain parts/area of the cell, all the while the sample are continuously imaged by fluorescence imaging. Observation on this bleached area would result in whether or not fluorescence on this area recovers over time.

Two proteins from two different cells are tagged by GFP, namely NE81 in *Dictyostelium discoideum* and Erg24 in yeast cells. NE81 is a lamin-like protein that associates with the inner nuclear envelope of *Dictyostelium* cells and plays a role in the formation of a nuclear lamina [28]. Erg24 is an enzyme that is involved in ergosterol/sterol biosynthesis [29]. It is a membrane protein mostly found in yeast, but also exist in other organism as well [30].

10.2 METHODS

FRAP measurements was conducted to two proteins (NE81 and Erg24, both tagged with GFP) in living cells. Experiment was conducted twice for each protein, yielding in two image series (movies) of each protein.

Data sampling of selected cells on the image series over time was done through imageJ (Fiji) and saved as csv files. These data are then combined (for both image series of one protein) and processed in a script written in  (available publicly on  GitHub, or by request).

The sampling procedure involves in measuring on a certain area (RoI - Region of Interest) the fluorescence intensity of:

- photobleached cells (two frames pre-bleaching and afterwards until the last frame)
- several unbleached cells (all frames)
- the background (all frames)

Calculation and plotting procedure involves several steps:

1. Averaging the background signal across all frames
2. Subtracting the fluorescence signal of the sampled cells by the background
3. Normalize the fluorescence signal of unbleached cells by the average measurements of the first two frames

4. Plot the unbleached measurements to obtain the slope for corrections
5. Normalize the fluorescence signal of photobleached proteins by the average measurement of the two frames pre-bleaching
6. Apply correction that is obtained by the slope of unbleached cells to the photobleached cells measurements
7. Average all corrected measurements of photobleached cells and plot against time

10.3 RESULTS AND DISCUSSION

As can be seen on the resulting FRAP plots (Fig. 10.3.1), the two proteins behave distinctly. It is evident that the measurement of NE81 does not recover the fluorescence over time, unlike the fluorescence of Erg24 that increases again.

Scrutinizing the plot in more detail, it can be seen in Fig. 10.3.1A that there are rather large errors of the fluorescent intensity measurement at certain time points. This wide error is due to the difficulty encountered during sampling using imageJ in which it is quite tricky to follow the ROI of the cells all across the time points of the image series, because the cells are moving everywhere along the 2D axes and also twisting around. And the fact that cells of this protein samples are quite small does not help the (manual) sampling using imageJ at all. This difficulty results in some outlying sampling data which widens the error bars. A closer inspection on the sampling data (shown by the black boxes in Fig. 10.3.1A) shows that a certain number of sampling could be done in a more accurate manner. However since the outlying sampling data were sparse and occurred on different sampled cells, taking into account that the final data would be constituted by the combined result of many sampled cells, no attempt or justification were made to neither remove any outlying data points nor resampling the image series. As can be demonstrated, all the calculation procedures were applied successfully, despite the relatively wide error bars on certain time points.

The resulting plot of NE81 shows that no recovery can be observed after photobleaching. This tendency is captured by the slope of the trendline (-0.00028) that indicates that the fluorescence signal stagnates, or even decreasing over time. This decrease can be attributed to natural occurrences that make fluorescence intensity decreases over time, even without bleaching, such as: exposure to light, molecules being destroyed, etc. The stagnation means that once the photobleaching occurred, NE81 proteins on the area get destroyed, but diffusion or transport of NE81 proteins from other parts of the cell does not occur. Literature suggest that the immobility of NE81 indicates that the cells in the sample are existing in the interphase, because NE81 are mobile during mitosis [28].

The plot of protein Erg24 (Fig. 10.3.1B) shows a different dynamic behaviour. Unlike NE81, the fluorescence signal increases over time, indicated by the slope of the trendline (0.0035). This increase is due to the diffusion or transport of proteins from other parts of the cells. The recovery of the fluorescence signal during the experiment does not return to the original intensity, probably due to the time frame of the experiment. Nevertheless, the movement of Erg24 proteins in photobleached cells is corroborated by literature as well [30].

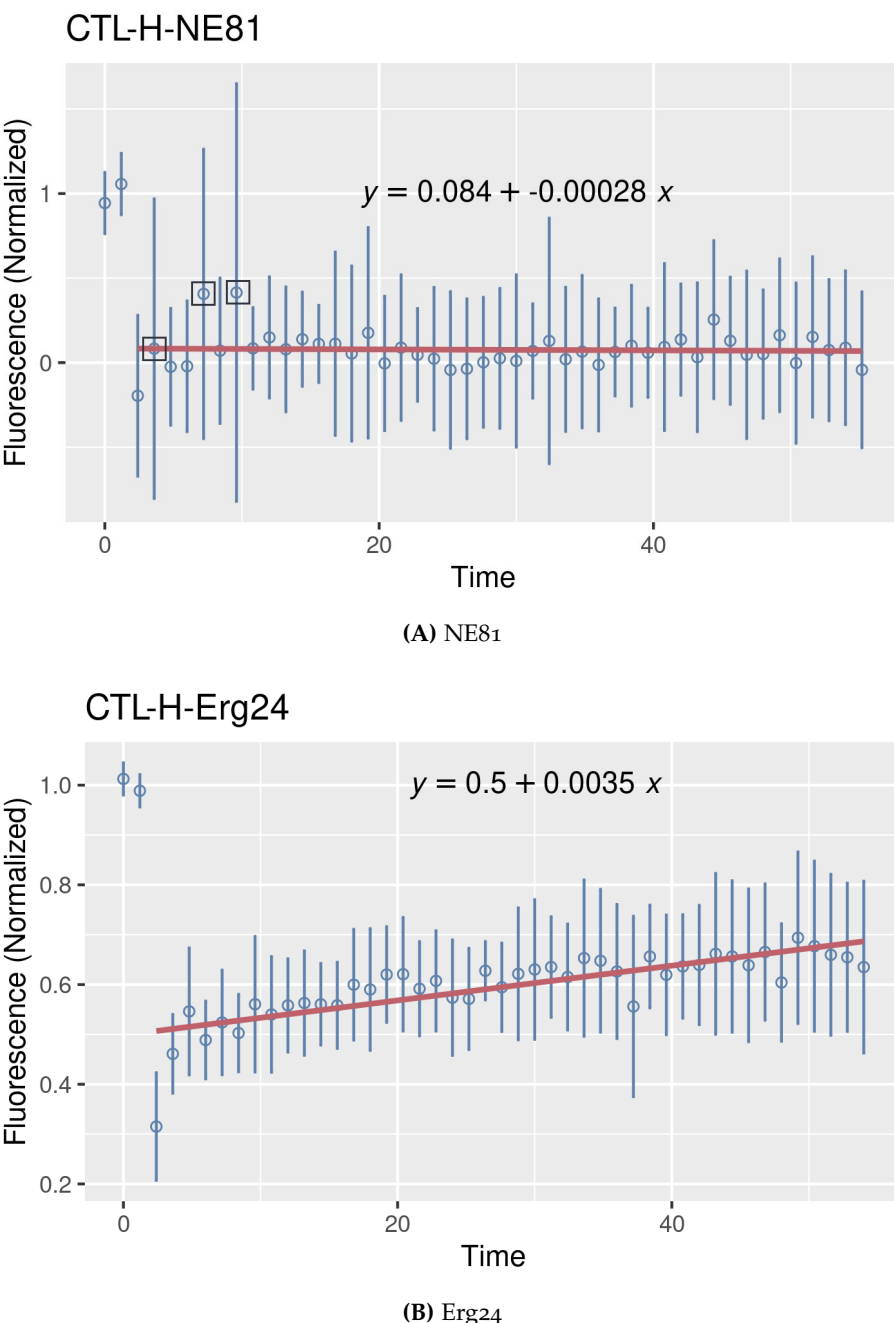


Figure 10.3.1: FRAP plot of the proteins NE81 (A) and Erg24 (B). Trendline is made from the datapoints, excluding the first two unbleached measurements. The slope (m) of the trendline for NE81 is -0.00028 and for Erg24 is 0.0035 . Boxes on A indicates the inspected sampling points.

The difficulty encountered during the sampling of NE81 proteins for the most part did not occur for this Erg24 protein, this is mostly due to the fact that the cells for this specimen are larger, and hence the bleached area can be tracked more accurately and also precaution has been taken after the sampling of NE81. This is reflected by the error bars of the measurement on each time point that do not indicate any significantly outlying sampling data.

The slope shown on the fluorescence recovery plots of both proteins, along with the trendline, are merely shown to help capture the tendency of how the fluorescence signal develops after photobleaching and does not in any way speculate about the

linearity of the datapoints. As indicated by the plot of Erg24 and the common fluorescence recovery curves, it is possibly not linear at all. Curve fitting to obtain the half-life of recovery ($t_{1/2}$) was not attempted because access to the software package of the microscope is limited at the time of writing this report [31].

In conclusion, it can be seen that the mobility of protein NE81 in *Dictyostelium discoideum* and Erg24 in yeast cells after photobleaching differs significantly, in which NE81 does not recover the fluorescence intensity signal and hence does not exhibit any movement, on the contrary, Erg24 recovers its fluorescence intensity signal in the area that is photobleached indicating that there is movement of the protein toward the photobleached area from other parts of the cell.

BIBLIOGRAPHY

- [1] R. Power and J. Huisken. "A guide to light-sheet fluorescence microscopy for multiscale imaging". In: *Nature Methods* 14 (2017), 360–373.
- [2] Michael Weber, Michaela Mickoleit and Jan Huisken. "Light sheet microscopy." eng. In: *Methods in cell biology* 123 (2014), pp. 193–215.
- [3] Jan Huisken et al. "Optical Sectioning Deep Inside Live Embryos by Selective Plane Illumination Microscopy". In: *Science (New York, N.Y.)* 305 (Sept. 2004), pp. 1007–9.
- [4] *Light Sheet Fluorescence Microscopy*. URL: <https://www.microscopyu.com/techniques/light-sheet/light-sheet-fluorescence-microscopy> (visited on 28/09/2021).
- [5] Alison J. North. "Seeing is believing? A beginners' guide to practical pitfalls in image acquisition ". In: *Journal of Cell Biology* 172.1 (Jan. 2006), pp. 9–18.
- [6] Otto Baumann. "Polarization DIC 2019". In: *Lecture slides* (2019).
- [7] *Pinhole Effect in Confocal Microscopes*. URL: <https://www.leica-microsystems.com/science-lab/pinhole-effect-in-confocal-microscopes/> (visited on 08/03/2021).
- [8] *Understanding the Digital Image*. URL: <https://www.zeiss.com/microscopy/int/solutions/reference/basic-microscopy/understanding-the-digital-image.html> (visited on 08/03/2021).
- [9] *Spectral Imaging and Linear Unmixing*. URL: <https://www.microscopyu.com/techniques/confocal/spectral-imaging-and-linear-unmixing> (visited on 25/09/2021).
- [10] Ralf Gräf. "Optical sectioning 2019 02". In: *Lecture slides* (2019).
- [11] *Introduction to Spectral Imaging and Linear Unmixing*. URL: <https://www.zeiss.com/microscopy/int/solutions/reference/spectral-imaging/introduction.html> (visited on 25/10/2021).
- [12] *Practical Aspects of Spectral Imaging*. URL: <https://www.zeiss.com/microscopy/int/solutions/reference/spectral-imaging/practical-aspects-of-spectral-imaging.html> (visited on 25/09/2021).
- [13] Kenneth N. Fish. "Total Internal Reflection Fluorescence (TIRF) Microscopy". In: *Current Protocols in Cytometry* 50.1 (2009), pp. 12.18.1–12.18.13.
- [14] Michael J. Sanderson et al. "Fluorescence microscopy." eng. In: *Cold Spring Harbor protocols* 2014 (10 Oct. 2014), pdb.topo71795.
- [15] Fei Chen, Paul W. Tillberg and Edward S. Boyden. "Optical imaging. Expansion microscopy". eng. In: *Science (New York, N.Y.)* 347.25592419 (Jan. 2015), pp. 543–548.
- [16] Joseph Huff. "The Airyscan detector from ZEISS: confocal imaging with improved signal-to-noise ratio and super-resolution". In: *Nature Methods* 12.12 (2015), pp. i–ii.

- [17] Annette Bergter and Joseph Huff. *ZEISS LSM 880 with Airyscan - Introducing the Fast Acquisition Mode*. Apr. 2016.
- [18] Ralf Gräf. "Optical sectioning 2019 01". In: *Lecture slides* (2019).
- [19] *TetraSpeck™ Microspheres, 0.2 µm, fluorescent blue/green/orange/dark red*. URL: <https://www.thermofisher.com/order/catalog/product/T7280#/T7280> (visited on 02/10/2021).
- [20] *Artifacts and Aberrations in Deconvolution Analysis*. URL: <https://www.olympus-lifescience.com/de/microscope-resource/primer/digitalimaging/deconvolution/deconartifacts/> (visited on 03/10/2021).
- [21] B. Zimmermann and B. Walz. "Serotonin-induced intercellular calcium waves in salivary glands of the blowfly *Calliphora erythrocephala*". In: *The Journal of Physiology* 500.1 (1997), pp. 17–28.
- [22] Md. Shahidul Islam. *Calcium Signaling*. Apr. 2012.
- [23] A. Z. Politi et al. "Quantitative mapping of fluorescently tagged cellular proteins using FCS-calibrated four-dimensional imaging". In: *Nature Protocols* 13 (2018), 1445–1464.
- [24] *RPL3 / YOR063W Overview*. URL: <https://www.yeastgenome.org/locus/S000005589> (visited on 20/10/2021).
- [25] Kirsten Bacia, Sally A. Kim and Petra Schwille. "Fluorescence cross-correlation spectroscopy in living cells". In: *Nature Methods* 3.2 (2006), pp. 83–89.
- [26] V. Dunsing et al. "Optimal fluorescent protein tags for quantifying protein oligomerization in living cells". In: *Scientific Reports* 8.10634 (2018).
- [27] Bo Yang Yu et al. "Image processing and classification algorithm for yeast cell morphology in a microfluidic chip". In: *Journal of Biomedical Optics* 16.6 (June 2011), pp. 1–10.
- [28] Anne Krüger et al. "Characterization of NE81, the first lamin-like nucleoskeleton protein in a unicellular organism". In: *Molecular Biology of the Cell* 23.2 (2012). PMID: 22090348, pp. 360–370.
- [29] *UniProtKB - P32462 (ERG24_YEAST)*. URL: <https://www.uniprot.org/uniprot/P32462> (visited on 08/02/2021).
- [30] Petros Batsios et al. "Nuclear envelope organization in *Dictyostelium discoideum*". In: *International Journal of Developmental Biology* 63 (2019), pp. 509–519.
- [31] Ralf Gräf. "Optical sectioning and 3-dimensional imaging - LCI". In: *Lecture slides - LCI* (2019).